THE EFFECT OF NANOSCALE SURFACE TOPOGRAPHY ON ADHESION,
PROLIFERATION AND PROTEIN EXPRESSION OF NEURONAL CELLS

A THESIS SUBMITTED TO
THE GRADUATE SCHOOL OF NATURAL AND APPLIED SCIENCES
OF
MIDDLE EAST TECHNICAL UNIVERSITY

BY

DİDEM MİMİROĞLU

IN PARTIAL FULFILLMENT OF THE REQUIREMENTS
FOR
THE DEGREE OF DOCTOR OF PHILOSOPHY
IN
BIOCHEMISTRY

MARCH 2022

Approval of the thesis:

THE EFFECT OF NANOSCALE SURFACE TOPOGRAPHY ON ADHESION, PROLIFERATION AND PROTEIN EXPRESSION OF NEURONAL CELLS

submitted by **DİDEM MİMİROĞLU** in partial fulfillment of the requirements for the degree of **Doctor of Philosophy** in **Biochemistry, Middle East Technical University** by,

Prof. Dr. Halil Kalıpçılar
Dean, Graduate School of **Natural and Applied Sciences** _____

Assoc. Prof. Dr. Özgül Persil Çetinkol
Head of the Department, **Biochemistry** _____

Assoc. Prof. Dr. Tülin Yanık
Supervisor, **Biochemistry, METU** _____

Assoc. Prof. Dr. Batur Ercan
Co-Supervisor, **Metallurgical and Materials Eng, METU** _____

Examining Committee Members:

Assoc. Prof. Dr. Salih Özçubukçu
Chemistry, METU _____

Assoc. Prof. Dr. Tülin Yanık
Biochemistry, METU _____

Prof. Dr. Ayşen Tezcaner
Engineering Sciences, METU _____

Prof. Dr. Emir Baki Denkbaş
Biomedical Engineering, Baskent Uni _____

Prof. Dr. Fatih Büyükserin
Biomedical Engineering, TOBB ETU _____

Date: 30.03.2022

I hereby declare that all information in this document has been obtained and presented in accordance with academic rules and ethical conduct. I also declare that, as required by these rules and conduct, I have fully cited and referenced all material and results that are not original to this work.

Name Last name : Didem Mimiroğlu

Signature :

ABSTRACT

THE EFFECT OF NANOSCALE SURFACE TOPOGRAPHY ON ADHESION, PROLIFERATION AND PROTEIN EXPRESSION OF NEURONAL CELLS

Mimiroğlu, Didem
Doctor of Philosophy, Biochemistry
Supervisor : Assoc. Prof. Dr. Tülin Yanık
Co-Supervisor : Assoc. Prof. Dr. Batur Ercan

March 2022, 81 pages

Neural guidance channels (NGCs) are tubular structures that are placed between distal and proximal ends of a damaged nerve to support the regeneration process. NGCs should support neural cell functions, conduct electrical impulses and have biomimetic surface characteristics. One of the approaches to attain these properties for NGCs properties is to use nanotechnology, which refers to altering physical and chemical properties of a material by controlling its size below 100 nm. There are various studies about the effects of submicron and micron sized surface features on the proliferation and biological functions of neural cells. However, studies concerning electrically conductive materials having surface features below 100nm are limited. For this reason, poly (lactic-co-glycolic) acid (PLGA), a currently-used material to fabricate NGCs, and a more accessible natural material, silk fibroin, were used to systematically obtain nanotopographical structures on their surfaces. This thesis provided data to the literature by comparing biological properties of PLGA films having 30 nm and 80 nm surface feature sizes. In addition, carbon nanofibres (CNFs) were incorporated as a secondary phase into silk fibroin films having nano

and sub-micron level surface features (50 nm and 125 nm) to provide electrical conductivity, then these surfaces were tested for proliferation, viability, functions and morphologies of neural cells using neuroblastoma cell line, N2a. Findings from this thesis aimed to pave the way for future NGCs to regenerate damaged neural tissue in patients having neural tissue injury.

Keywords: nanostructure, neural cells, N2a, surface topography, conductivity

ÖZ

NANOBOYUTLU YÜZEY PÜRÜZLÜLÜĞÜNÜN NÖRAL HÜCRELERİN YAPIŞMASINA, ÇOĞALMASINA VE PROTEİN EKSPRESYONUNA OLAN ETKİSİNİN İNCELENMESİ

Mimiroğlu, Didem
Doktora, Biyokimya
Tez Yöneticisi: Doç. Dr. Tülin Yanık
Ortak Tez Yöneticisi: Doç. Dr. Batur Ercan

Mart 2022, 81 sayfa

Sinir yönlendirici kanallar (SYK'lar) hasarlı sinirin proksimal ucu ile distal ucu arasına yerleştirilen ve rejenerasyon sürecini destekleyen kanal yapılarıdır. SYK'lar, nöral hücre fonksiyonlarını destekleyen; iletken ve biyolojik yapılara benzer özelliklere sahip olmalıdır. SYK`lar üzerinde bu özellikleri elde etmek için yaygın bir şekilde kullanılan yöntemlerden biri de malzemenin fiziksel ve kimyasal özelliklerinin, malzeme boyutlarını 100 nm'nin altında kontrol ederek farklı uygulamalar için kullanılmasını ifade eden nanoteknolojidir. Literatürde mikron altı boyutlu ve mikron boyutlu pürüzlülük içeren malzeme yüzeylerinin sinir hücrelerinin çoğalması ve biyolojik işlevleri üzerindeki etkilerini inceleyen çeşitli çalışmalar bulunmaktadır. Ancak yüzeylerinde 100 nm'nin altında boyutlara sahip yapılar içeren iletken malzemelerle ilgili çalışmalar oldukça sınırlıdır. Bu nedenle, SYK'ların üretiminde sıklıkla kullanılan poli (laktik-ko-glikolik) asit (PLGA) ve bu malzemeye göre daha kolay erişilebilir olan ipek fibroinin kullanılması ve bu yüzeyler üzerinde sistematik olarak nano boyutlu yapıların elde edilmesi üzerine

çalışılmıştır. Elde edilen nano boyutlu (30 nm ve 80 nm) yapılara sahip PLGA filmlerle karşılaştırma yapılarak literatüre yeni veriler kazandırılmıştır. Ayrıca ipek fibroin malzemesine elektriksel iletkenlik kazandırabilmek için ikincil bir faz olarak karbon nanofiber (KNF'ler) eklenmiş ve ardından yüzeyler üzerinde farklı nano ve mikron altı boyutlu yapılar (50 nm ve 125 nm) oluşturulmuştur. Elde edilen bu yüzeyler üzerinde nöral hücre çoğalması, canlılığı, fonksiyonları ve morfolojileri nöroblastoma hücre hattı, N2a kullanılarak incelenmiştir. Tezden elde edilen sonuçlarla geliştirilecek SYK'ların ileride sinir hasarı yaşayan hastalarda doku jenerasyonunun gerçekleşmesine katkıda bulunması amaçlanmaktadır.

Anahtar Kelimeler: nanoyapı, sinir hücresi, N2a, yüzey topografisi, iletkenlik

This doctoral thesis is dedicated to the young people who build their ideals on the everlasting future of the Republic of Turkey, work for this future and always live in hope…

ACKNOWLEDGMENTS

Lastly, I want to express my endless gratitute to my mother Sevgi Mimiroğlu and my father Bulut Ömer Mimiroğlu for their endless love, patience, supports and sacrifices in my work, ideals and future.

TABLE OF CONTENTS

LIST OF TABLES

TABLES

LIST OF FIGURES

FIGURES

LIST OF ABBREVIATIONS

ABBREVIATIONS

AAO	anodic aluminum oxide
AFM	atomic force microscopy
ALLO	allopregnanolon
BDNF	brain-derived growth factor
BSA	bovine serum albumin
BMSC	bone marrow-derived stromal cell
CNF	carbon nanofiber
CNS	central nervous system
CNT	carbon nanotube
dNSCs	differentiated neural stem cells
DMEM	Dulbecco's Modified Eagle Medium
DOPA	3,4-dihydroxyl-L-phenilalanin
DTT	dithiothretiol
ECM	extracellular matrix
FBS	fetal bovine serum
FDA	U.S. Food and Drug Administration
FTIR	Fourier-Transform Infrared Spectroscopy
GABA	gamma aminobutyric acid
GelMA	gelatin methacryloyl

GO	graphene oxide
HC	honeycomb
HdFib	human dermal fibroblast cell line
HFLP	hexafluoro-2-propanol
hMSCs	human mesenchymal stem cells
hour	h
MAPK	mitogen-activated protein kinase
MAP2	microtubule associated protein 2
min	minutes
MTT	3-4,5-dimethyl-thiazolyl-2,5-diphenyltetrazolium bromide
NGF	neural growth factor
NSc	neural stem cell markers
NGCs	neural guidance channels
N2a	mouse neuroblastoma cell line, Neuro2-a
PBS	phosphate buffer saline
PCL	poly (ε-caprolactone)
PEG	polyethylene glycol
PF-NGC	porous flat nerve guidance channel
PGA	polyglycolic acid
PLA	poly (lactic acid)
PLCL	poly-DL-lactic-co-caprolactone
PLGA	poly (lactic-co-glycolic) acid

PNI	peripheral nerve injury
PNS	peripheral nervous system
PP-NGC	porous pattern nerve guidance channel
PS	penicillin/streptomycin
PU	polyurethane
PUA	polyurethane acrylate
PVA	polyvinyl alcohol
RT	room temperature
SD	standart deviation
SEM	scanning electron microscopy
SS	stainless steel
XPS	X-ray photoelectron spectroscopy
3D	three-dimensional

CHAPTER 1

INTRODUCTION

A worldwide effort was given to the brain research in the past years. The initiatives are bold but mainly includes the brain mapping in detail, understanding the cell types and their activity and interconnections [1]. This will also improve the studies about the treatment of neuronal damage diseases which can also promote a level of cooperation that will bring an interdisciplinary perspective to fundamental problems in neuroscience. The nervous system has a vital role based on coordinating, making communication and responses between the body system and the environmental changes and stimulation. There are two major parts of the nervous system which are the central nervous system (CNS) and the peripheral nervous system (PNS). The brain and spinal cord are associated with the CNS, while the PNS includes the nerves that extend from the CNS towards the body [2]. There are many factors that can damage both the CNS and PNS, including chemical, mechanical and ischemic factors. On the other hand, both nervous systems differ in their recovery response when exposed to damages. It is not spontaneously possible for neural cells to regenerate themselves for CNS upon damage [2,3]. On the other hand, the self-renewal property of neuronal cells (axonal regeneration) in the PNS vary.

1.1   Peripheral Nerve Injury and Neural Guidance Channels

Injuries in the PNS is one of the major public health problems in the worldwide [4]. Peripheral nerve injury (PNI) is a clinical chronic trauma which is very common and major problem resulted with partial or complete sensory impairment and dysfunctions. There are many common factors resulting in PNI, such as accidents, various medical conditions and autoimmune diseases. Each year, about 200.000 and 300.000 individuals are diagnosed with PNI in the United States and Europe,

respectively [2,5]. Although damaged peripheral nerves have a capacity for self-healing to a certain extent after injury, it can take a very long time depending on the age and other overall health of the patient, the length of the nerve gap and environmental factors (type, size and location of the injury) in the damaged area [2,6]. In fact, patients suffering from PNS injuries can wait for years for some level of recovery and, at the end, may be left with devastating sensory and motor deficits which renders them disabled [7].

There are two commonly-used treatment methods for damaged peripheral nerves: non-surgical and surgical treatments. While electrical and magnetic stimulation and application of nerve growth factors are classified as non-surgical treatments, nerve grafting is most commonly used for the surgical treatments, such as autografting, allografting and xenografting [8]. These grafting methods are typically used for treatments in PNS injuries larger than 1.5 - 3 cm [8–10]. However, these treatment options all have their drawbacks. Autografting, which is the gold-standard treatment for PNS injuries, requires the sacrifice of a donor nerve and can lead to donor site morbidity, pain and neuroma. The limited availability of autografts is also problematic for severe nerve injuries requiring grafting to multiple anatomical locations. For the case of allografts, there are not sufficient number of available donors, while allografts and xenografts can both induce immune response in the recipients potentially lead to disease transmission form donors to the recipients [10]. These complications limited the use of autografts, allografts and xenografts and led to the development of nerve guidance channels (NGCs) for the treatment of PNS injuries. NGCs are tubular shaped hollow structures bridging the distal and proximal stumps of injured neurons [8]. The ends of the injured nerve stumps can be affixed into the ends of the tube and provides an isolated pathway conducive to regeneration (Fig. 1) [11,12]. NGCs direct axons sprouting from the proximal nerve stump, provide a conduit for the diffusion of growth factors secreted by the injured nerve ends and reduce the infiltration of scar tissue [13].
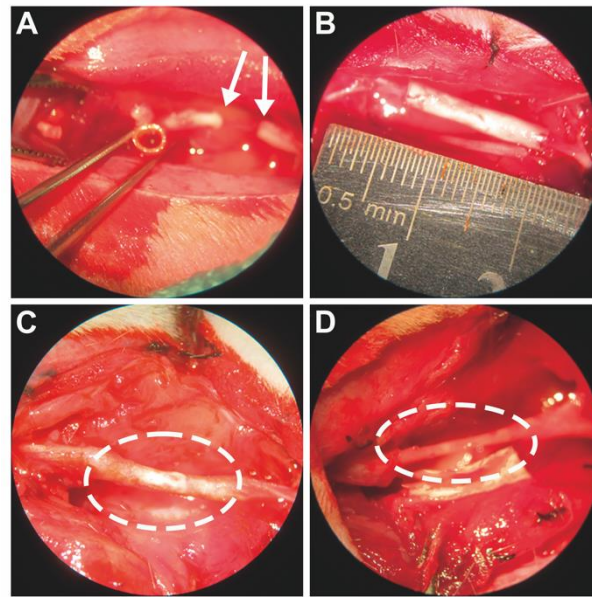
Figure 1. A rat sciatic nerve and surgical implantation of nerve conduits
A) Photo of nerve conduits between tweezers and a rat sciatic nerve defect that was showed with white arrows, B) conduit ingrafted to the nerve defect, C) photo of the conduit and D) regenerated nerve defect after 6 weeks implantation. Reproduced with permission from Huang et al., 2015. [11]

NGCs aim to facilitate cellular migration, spreading and provide a growth area for the damaged neural tissue in all dimensions. For this reason, these channel systems should have basic features that will accelerate the healing of the damaged area correctly. NGCs should be biocompatible without making any inflammatory responses and immunological reactions. One of the important properties for the NGCs is biodegradability. The ideal degradation rate should be similar with healing rate of damaged nerve [2,8,14]. There are various studies in literature investigating the use of biocompatible and biodegradable materials for NGC applications. Silk-fibroin, alginate, chitin and chitosan, type I collagen, hyaluronic acid derivatives and keratin are materials which have a natural-origin, whereas poly (lactic acid) (PLA), polyvinyl alcohol (PVA), poly glycolic acid (PGA), poly (lactic-co-glycolic acid) (PLGA), polyurethane (PU), polyethylene glycol (PEG) and polycaprolactone (PCL) are synthetic materials used for NGC applications [2,14–18]. In fact, the use of these materials as NGCs enhanced neural cell functions *in vitro* and translated into

improved motor functions *in vivo* [19]. Another important characteristic of materials used for NGCs should be the lack of inflammatory response from its degradation products. Permeability is another crucial property to design NGCs, providing sufficient permeability via porous surfaces on NGCs facilitate oxygen, growth factors and nutrient diffusion to the damaged area [20].
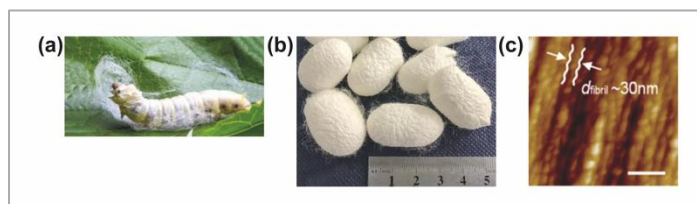
Figure 2. Silk fibroin. a) *Bombyx mori* silkworm, b) the silk cocoon of *Bombyx mori* silkworm (Tufan, 2020) [61] c) AFM micrograph of silk fibroin fibrils (Xu et al., 2014) [108].

Among the aforementioned materials, silk fibroin is an important natural fibrous material used in neural tissue engineering. Silk fibroin material consists of the fiber protein, silk fibroin produced by the silk worm *Bombyx mori* [21]. Due to its physicochemical, mechanical and biological properties, silk fibroin can be processed easily and fabricated in film, porous scaffold, gel and mat (straw) structures, and thus it is frequently used in biomedical applications [22,23]. Silk fibroin, which is an FDA approved material, demonstrated to have a low inflammatory response and antigenicity compared to other biodegradable polymers [24]. It was shown in literature that silk fibroin supports cellular attachment and proliferation of neurons and Schwann cells, as well as primary cells and different cell lines [22,23]. Gennari et al. (2017) evaluated silk fibroin scaffolds functionalized with gamma aminobutyric acid (GABA) and allopregnanolone (ALLO) for their performance in tissue engineering and nerve regeneration. It was shown that scaffold did not cause any inflammation after 1- and 3-month implantation *in vivo* and they were found to be biocompatible. Dorsal root ganglion cells cultured *in vitro* up to 5 days showed proper neural morphology and axonal elongation on the scaffolds. The proliferation of Schwann

cells increased 2-folds on silk-containing surfaces at the end of the 16 days [25]. In another study by Zhang et al. (2012), three-dimensional (3D) silk scaffolds with channel structures were fabricated and bone marrow-derived stromal cell (BMSC) and hippocampal neurons cultured on these surfaces were examined. According to the cell proliferation analysis performed, it was shown that silk scaffolds having 5% (wt) silk fibroin solution was effective and increased BMSC proliferation by 4-folds and enhanced multipolar morphology of hippocampal neurons at 7 days *in vitro*. In another study identified hippocampal neurons to form axonal structures at 7 days of culture on 3D silk scaffolds with a channel diameter of approximately 120 μm and cell-cell and cell-matrix interaction were found to be crucial for axon formation [23].

Silk fibroin can be fabricated in film, scaffold, gel forms depending on its favorable properties (Fig. 2). However having low electrical conductivity limits its use in the bone, muscle and neural tissue engineering [26]. Due to having low conductivity, silk fibroin can be supported with carbon based materials including using carbon
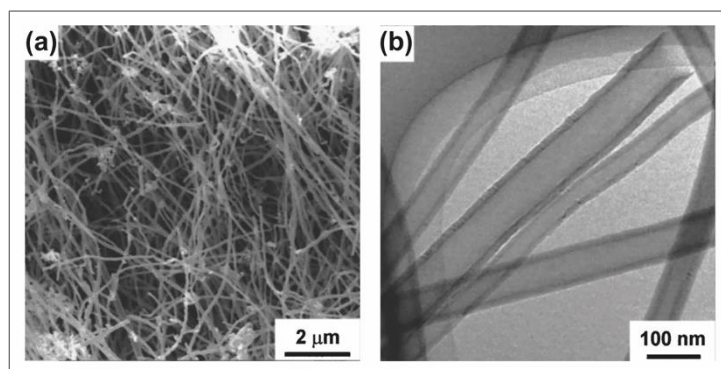
Figure 3. Carbon nanofiber. a) The image of nanofibers taken by FE-SEM and b) the image of uncoated nanofiber by TEM (Endo et al., 2002) [109].

nanotubes (CNTs), carbon nanofibers (CNFs), graphene oxide, silver and gold nanoparticles to enhance its electrical properties [26,27]. Among these secondary phase additives, CNF is a type of carbon fiber structure having nano scale dimensions that can be fabricated with various techniques, including chemical vapor deposition (CVD), which was the fabrication method used for CNFs in this thesis. CNFs fabricated with CVD are cheaper, less toxic, easily functionalized, easier to dissolve in solution, have high electrical and thermal conductivity and excellent mechanical

5

properties compared to carbon nanotubes (CNTs) [26]. In a study by Naskar et al. (2016), the silk fibroin-CNF nanocomposite scaffolds were tested for their biocompatibility with L929 (mouse fibroblast cell line) and HdFib (human dermal fibroblast cell line). While HDFib cells showed a 5-fold increase at the end of the 10 days with silk fibroin-1.0CNF (100/5, the mass ratio) concentration, it was found significant compared to the control group, only silk fibroin. For the L929 cells, a 5-fold increase was observed at the end of the 5 days *in vitro* [26]. In another study, conductive nanocomposites were prepared with silk fibroin using gold nanorods and evaluated for their use in neural tissue engineering (Afjeh-Dana et al., 2019). Results showed that PC12 proliferation and viability decreased approximately 20% on the samples containing only silk fibroin, whereas the cells remained in the same viability on silk fibroin nanorod composite samples up to 14 days of culture [27]. While there are a lot of studies for CNF incorporation into various polymers for bone and cardiac tissue engineering applications, there are no studies on neural tissue engineering with silk fibroin CNF composites [28,29]. In addition, there are several studies in literature on the effects of nanotopographical structures for neural cells. By evaluating these studies, it is possible to have an idea about the favorable effects of these structures on neural cells.

In addition to the aforementioned properties, such as biocompatibility, biodegradation etc., another significant property for NGCs is promotion of cellular support via adhesion and proliferation. These properties are mostly related with material surfaces. For this reason, different surface modifications such as chemical adsorption, plasma treatment, layer-by-layer assembly, molecular imprinting etc. were performed on material surfaces for neural tissue applications to maximize neural cells and tissue interactions [30]. In addition to these modifications, nanoscale dimension have an important role in the preparation of the NGCs which may guide growing the damaged axon from the proximal end to the distal end. Having these additional nanotopographical structures, cells can easily migrated to the damaged area, the cell-cell interactions and neurite alignment can be supported.

In addition, another important requirement is having electrically conductive for NGCs [8]. Having some of these properties, various materials are clinically approved by the Food and Drug Administration (FDA), USA for NGCs applications, i.e. Neuragen®, NeuraWrap™, Neuromend™, Neuromax and Neuromatrix/Neuroflex™ composed of collagen, Neurotube® composed of polyglycolic acid (PGA), Neurolac™ composed of poly-DL-lactic-co-caprolactone (PLCL) and Salubridge and SaluTunnel composed of polyvinyl alcohol (PVA) [8,14,18,31]. Among these products, there are many studies to develop with having all significant properties and better NGCs, since there is no perfect NGCs with all properties. On the other hand, there are some general features that NGCs should have, such as topographical structures on surfaces and conductivity for facilitating cellular adhesion, migration and neuronal activity, respectively [32].

1.2   Topographical Structures and Conductivity

Nanotechnology refers to the use of chemical and physical changes in materials to fabricate new and different technological products by controlling the size of a material under 100 nm, and materials in these dimensions are called 'nanomaterial' [33]. In biological systems, interactions of proteins, carbohydrates, lipids and glycosaminoglycans in extracellular matrix (ECM), and interaction of cell-cell and cell-tissue occur in nanodimension. Therefore, materials used in biological systems should be designed to possess nanoscale topography. This property allows cells and tissues to interact with a surface that mimics its natural microenvironment and these materials are called as biomimetic materials. Nanopillars, nanopits, nanogrooves, and nanopores can be given as examples for these nanotopographical structures [34].

There are many studies about the effects of nanotopography on the function of cells and tissues, especially bone tissue. Orthopedic studies focus on regenerating damaged bone and cartilage tissue in the skeletal system. Due to long healing period of damaged areas, material properties of the implant systems are important. One of the most important requirements is the longevity of these implants without triggering

any immune response, especially for the intraosseous applications. To enhance the longevity of the implants, different nanostructures were fabricated on titanium implant surfaces and then, they were tested with macrophages to evaluate immune response. It was observed that the implant with 80 nm nanotopographical surface (NT20) stimulated macrophage cells 4 times more than the implant with 30 nm nanotopographical surface (NT5). At 8 weeks after implantation, there was 20% more osseointegration between bone and implant for NT5 compared to NT20 [35]. Ballo et al. (2011) assessed the effect of titanium implants with different nanodimensional surfaces (60 nm, 120 nm, 220 nm) in rat tibia. It was observed that the bone-implant interaction in the implant surfaces with 60 nm sized nanostructures (76%) was higher than the 120 nm (45%) and control (57%) ones [36].

Another biological system where the use of nanomaterials is examined is vascular stents. There are various studies about the response of the endothelial cells interacting with nanotopographical surfaces. For this purpose, they fabricated nanotopographies less than 50 nm on titanium surfaces (N-Ti), and tested with rat aortic endothelium cells and rat aortic smooth muscle cells together (as a co-culture) and separately. At the end of 2 weeks, it was observed that N-Ti surfaces interacting with rat aortic endothelial cells increased collagen synthesis 2 times and elastin synthesis nearly 10% compared to the control group (F-Ti, flat Ti). It was also observed for rat aortic muscle cells that collagen synthesis increased 20 to 40% and elastin synthesis increased up to 50% on N-Ti surfaces compared to the control group. As a result, nanotopographical changes on titanium surfaces had a significantly different response on endothelial cells than smooth muscle cells [37].

Some studies also investigated the effects of surface modifications on polymeric materials for cellular functions. Giavaresi et al. (2006) showed and studied the natural polyester (Biopol[TM]) 3-hydroxybutyrate-co-3-hydroxyvalerate (3HB-3HV) containing 8% 3-hydroxyvalerate component (D400G) and biodegredable polycaprolactone (PCL) efficiency. Nanopits with 100 nm depth and 120 nm diameter were obtained on D400G surfaces and nanopillars with 160 nm depth and 100 nm diameter were obtained on PCL surfaces. *In vitro* experiments using L929

fibroblast cells demonstrated significant differences in the release of pro-inflammatory cytokines among the sample groups. It was observed that the polymers having nanoscale roughness on their surfaces had less pro-inflammatory cytokine levels compare to the ones lacking nanoscale roughness on their surfaces [38].

Systematic changes in the nanoscale surface topography provided differences in cellular functions and differentiation. Oh et al. (2009) showed that osteogenic differentiation of human mesenchymal stem cells (hMSC) on nanotubular titanium oxide structures with varying size (30 nm, 50 nm, 70 nm and 100 nm) occured using medium without any osteogenic cell-inducing factors. It was observed that on the nanotubular structures having 30 nm and 50 nm sizes induced more frequent protein clusters compared to the one having 70 nm and 100 nm nanotubular structures. It was speculated that nanotubular structures having 70 nm and 100 nm sizes had wider porosity, thus protein clusters were reduced on the surface. Protein clusters also affected cellular morphology, where hMSCs stretched and elongated to find protein clusters on nanotubular surfaces. As a result, hMSCs could more easily differentiate into osteoblasts. Additionally, since there was a large amount protein clusters on nanotubular surfaces on samples having lower diameter, hMSC adhesion and proliferation increased. In other words, the adhesion, elongation and differentiation behaviors of hMSCs were shown as a function of the size of nanotubular structures obtained on the surface, and it revealed that the geometric differences on the material surface had a specific mechanism which was effective on stem cell differentiation. According to these proposed mechanism, as summarized in Fig. 4, hMSC differentiation decreased, while their adhesion and proliferation increased with a decrease in nanofeature dimensions. On the other hand, when the stem cells were under metabolic stress, they could differentiate to specific cell types to control this stress situation [39]. Although interaction of nanotopograhical surfaces with different

cells were investigated in various studies, neural cells and neural cell functions were not evaluated upon the control of nanofeature size in a range less than 100 nm.

For neuronal cells, most of the published studies investigating the interactions between neural cells and materials surfaces focus on "micron" scale surface topography [40–43]. Tsuruma et al. (2008) prepared honeycomb (HC) pores with dimensions changing from 3 to 15 µm on films prepared from poly(Ɛ-caprolactone) (PCL) and amphiphilic polymer mix (a copolymer of dodecylacrylamide and ω-carboxyhexylacrylamide (Cap)) to control neural stem cells. Neural stem cells isolated from cerebral cortex of mice were seeded on these films, followed by staining with Nestin and MAP2 (microtubule associated protein 2) to evaluate stem cell differentiation. The degree of differentiation on HC films was expressed in terms of the number of cell positive for MAP2 and Nestin and the results showed that there were nearly 81.6% mature neural cells coated on flat surfaces. There were 55.3, 31.9 and 12.9 % neural stem cell, immature neural cell and mature neural cell on HC films, respectively. As pore size increased from 8µm to 15µm, the degree of differentiation toward neural cells increased by an equal percentage. This was the first study assessing the influence of altered HC film pore size to control neural cell differentiation. Pore size of HC films were identified as a potential means to control stem cells differentiation and the neural cell extensions. It was also stated that HC films could be a potential material for cell therapy and the cell transplantation in neural tissue engineering [44]. In addition, pillars and grooves having 300 nm to 1500
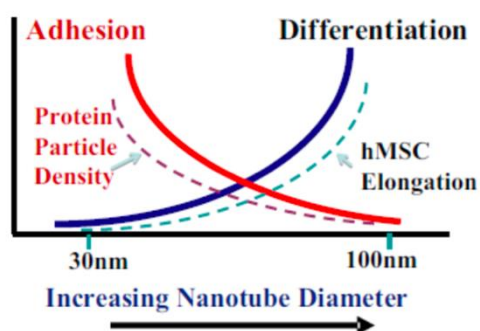
Figure 4. The effects of changing nanotubular structures on the fuctions of human mesenchymal stem cells. Reproduced with permission from Oh et al., 2009. [39]

nm feature size were obtained on polyurethane acrylate (PUA) covered with fibronectin, and the effect of surface features on human neural stem cell differentiation was evaluated by Tuj1 (neural cell marker) and GFAP (astrocyte marker) gene expression levels. It was observed that cells did not align properly on the smooth surfaces, however cellular radial aligned was observed on pillar nanopatterned surfaces. They found that Tuj1 and GFAP expression levels were higher on nanotopographical surfaces than smooth surfaces and the highest gene expression level was found on 300 nm nanotopographical surfaces [45]. In another study, PLGA samples were coated with 3,4-dihydroxy-L-phenilalanin (DOPA) and grooves having 5 μm, 800 nm to 400 nm topographical scales were obtained. Independently of the presence of DOPA on surfaces, neural cell extension was found to be longer on surfaces with 400 nm topographies than the smooth ones [46]. To mimic the natural arrangement of ECM and axons in neural tissue, different forms of multichannel lumens were preferred [47]. A gelatin-based multi-channeled scaffold enriched with the neurotrophic factors NGF and BDNF was designed to create dual growth factor delivery. It was observed that aligned nanofibers were more effective in guiding differentiated neural stem cells (dNSCs) compared to non-aligned nanofibers. Additionally, cellular density and neurite length increased while NGF concentration increased [48]. In another study, decreasing scar tissue formation for electrodes implanted in the brain or spinal cord was investigated. Anodic aluminum oxide (AAO) surfaces were used as electrodes to obtain small pores (about 20 nm) and larger pores (about 90 nm). It was found that astrocytes adhesion was higher on small pore structures than larger pores (Fig. 5). Similarly, astrocytes formed focal adhesions on small pores. Additionally, GFAP expression level of astrocytes was lower on surfaces having small pores [49].
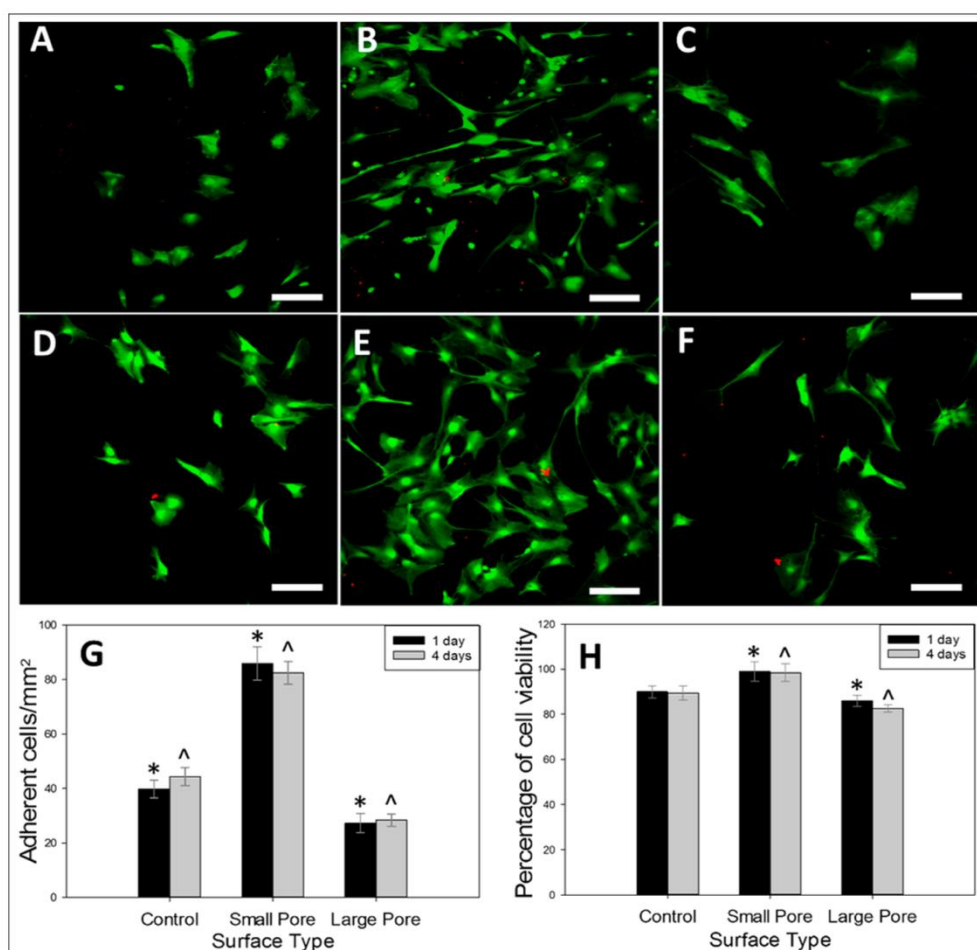
Figure 5. Cellular adhesion and cell viability results on AAO surfaces with small pores and large pores. The merged images of astrocytes stained with calcein (green) and propidium iodide (red) for the control (A, D), small pores (B, E), and large pores (C, F). Top row images were at 1st day and bottom row images were 4th day of culture (Ganguly et al., 2017) [49].

In another study, axonal elongation and cellular migration were characterized on PLGA polymer having microgrooves and microporousity. They fabricated both porous flat (PF-NGC) and porous patterned nerve guidance conduits (PP-NGC) with 5 μm sized surface micropatterns. It was observed that the migration speed of PC12 cells on PP-NGC surfaces was twice higher than PF-NGC surfaces after 48 hours of culture. Cells were observed to elongate three times higher on PP-NGC was than PF-NGC samples [20].

In literature, it was demonstrated that conductivity was important for neuronal cells due to having a positive effect on neuronal cells in terms of neurite outgrowth, cellular movement and neural differentiation [50]. Wang et al. (2020) designed conductive Au-PCL scaffolds and provided electrical stimulation to evaluate PC12 cellular functions. The results showed that 80 nm Au coated PCL scaffolds had the highest neurite length and neurite number per cell. Neurites lengths were about 15 times and neurite numbers were about 4 times higher for 80 nm Au-PCL compared to PCL group [51]. In another study, Park et al. (2020) fabricated conductive hydrogel NGCs using gelatin methacryloyl (GelMA) and graphene oxide (GO) for peripheral nerve regeneration. It was observed that while cell densities were found similar on GelMA, GO/GelMA and r(GO/GelMA) at 5th day *in vitro*, the number of neurite bearing cells was 1.5-folds and 2-folds higher for GO/GelMA and r(GO/GelMA) compared to the control group, GelMA, respectively [52].

In literature, it was observed that nanoscale structures play a crucial role for the adhesion, differentiation and migration of the cells due to mimicking ECM properties for different cell types. In peripheral nervous system, peripheral nerves contain nerve fibers which are surrounded by connective tissue (endoneurium, perineurium and epineurium) and blood vessels (Arslantunali, 2014). Each endoneurium is composed of axons and Schwann cells that produce myelin sheaths, and endoneurium are surrounded by perineurium. Finally, perineurium and blood vessels are located together that are surrounded by epineurium (Fig. 6) (Arslantunali, 2014; Nawrotek, 2015).
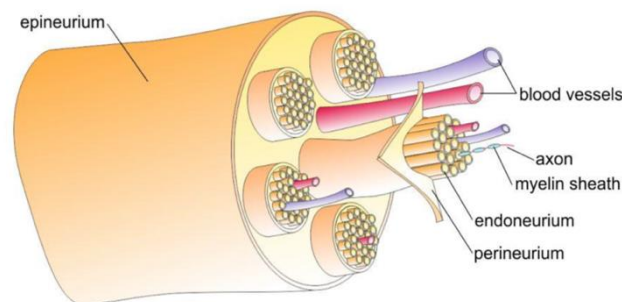
Figure 6. Structural organization of the peripheral nerve in peripheral nervous system. Reproduced with permission Nawrotek, 2015. [110]

In the endoneurium, axons are embedded in a connective tissue which contains type I and III collagen molecules. Collagen is composed of three distinct **α**-chains that are closely packed in helical conformation. Additionally, the thickness of collagen is 15 Å (1.5 nm) and the cross-striations on collagen molecules are in 640 Å (64 nm) in size [55]. Moreover, in endoneurium, Schwann cells are surrounded by the basal lamina. This basal lamina is composed of type IV collagen, laminin, heparan sulfate proteoglycan and fibronectin molecules. Polylaminin structure has hexagon-like morphology whose sides were nearly 30 nm [56]. Having this said, length and width of fibronectin protein are 15.5±1.3 nm and 8.8±1.7 nm, respectively [57], while heparan sulfate proteoglycan has a long protein core of 80 nm [58].

As it is mentioned above, mimicking neural cell environment on the surfaces by physical and chemical changes significantly enhance the cellular functions. Therefore, different properties should be precisely gained to the materials for the deeper understanding of cellular functions and obtaining new materials for NGCs applications.

1.3   Research and Thesis Organization

The main objectives of this thesis are:

1. Investigating the neuronal cell behaviour (adhesion, proliferation and protein expression) upon their interaction with nanoscale topographies in different size scales (30 nm and 80 nm) on PLGA surfaces.

2. Investigating the neuronal cell behaviour (adhesion, proliferation, protein expression and migration) upon the cellular interactions with needle-like nanotopographies in different size scales (50 nm and 125 nm) on conductive silk fibroin/CNF surfaces.

The organization of the thesis can be summarized as following:

This thesis consists of 5 chapters. In Chapter 1, PNS and NGCs were introduced and the main properties of NGCs were explained. Additionally, current studies focusing on the effects of surface topography and electricial conductivity and their applications for neural tissue generation were explained. In Chapter 2, materials and methods used for the experiments were detailed. In Chapter 3, surface characterization of PLGA films and the effects of nanoscale surface topography on neuronal cells were examined by assessing cellular adhesion, proliferation and protein expression levels. In the 4th chapter, surface characterization of silk fibroin/CNF films and the dual effect of electrical conductivity and nanoscale surface topography were evaluated by determining cellular adhesion, proliferation, protein expression levels and migration results. Finally, in Chapter 5, overall discussion of the previous chapters were provided. In addition, future and suggested studies were also discussed.

CHAPTER 2

EXPERIMENTAL METHODS

2.1   Materials

PURASORB® poly (lactic-co-glycolic acid) (w/w, 50:50) was provided by Corbion Purac (Amsterdam, The Netherlands). Cocoons by *Bombyx mori* were purchased from Kozabirlik (Bursa, Turkey). 3-4,5-dimethyl-thiazolyl-2,5-diphenyltetrazolium bromide (MTT), 4',6-diamino-2-phenylindole (DAPI), hexamethyldisilazane (HMDS), lithium bromide (LiBr), sodium carbonate (Na_2CO_3), methanol (CH_3OH), 1,1,1,3,3,3-hexafluoro-2-propanol (HFIP) and bovine serum albumin (BSA) were purchased from Sigma-Aldrich (Germany). Cytopainter Staining Kit (ab112127), anti-vinculin primary antibody (ab129002, rabbit monoclonal), Alexa Fluor 488 secondary antibody (ab150077, goat anti-rabbit), anti-c-fos primary antibody (ab222699, rabbit) anti-MAP2 primary antibody (ab32454, rabbit) and peroxidase linked secondary antibody (ab6721, goat anti-rabbit IgG) were purchased from Abcam (Cambridge, UK). β-actin primary antibody (PA1183, rabbit), M-PER™ Mammalian Protein Extraction Reagent and Pierce™ Coomassie Protein Assay Kit were purchased from Thermo Fisher Scientific (Massachusetts, USA). Clarity™ Western ECL Substrate was purchased from Bio-Rad Laboratories (USA). Protease inhibitor cocktail tablets (Roche Complete Mini EDTA-free) were purchased from Roche Diagnostic Gmbh (Germany). Dithiothreitol (DTT) was purchased from Thermo Fisher Scientific (Massachusetts, USA).

2.2   Preparation of PLGA Films with Nanoscale Topographies

PLGA films having nanoscale surface topographies were fabricated utilizing anodized 316L stainless steel (SS) surfaces as casting molds. To fabricate the molds, firstly, 316L SS foil (thickness 0.5 mm) was cut into 2.5 x 2.5 cm squares, followed by cleaning in acetone, 70% ethanol and ultrapure water each for 15 minutes (min), respectively. To obtain nanoscale topography on 316L SS surfaces, the surface cleaned samples were anodized. For the anodization process, 5% (v/v) perchloric acid in ethylene glycol solution was used as an electrolyte and the temperature of the system was kept between 0-10 ^{o}C range. A platinum mesh was used as the cathode and the 316L SS sample was the anode. 316L SS samples were anodized under 35 V for 5 min and 50 V for 6 min to obtain nanopit surface morphologies having different array sizes.[59] The anodized 316L SS samples were washed with ultrapure water and dried at room temperature (RT).

Once 316L SS samples having nanopit surfaces were fabricated, they were used as molds to transfer their nanoscale surface topographies onto PLGA films. PLGA (50:50, molar ratio) was dissolved in chloroform to obtain 8% (w/v) solution and poured onto anodized 316L SS. The PLGA solution poured onto 316L SS allowed to evaporate for 1 hour (h) at RT and 48 h inside an oven at 37 ^{o}C to remove the chloroform [60]. Afterwards, PLGA films were peeled from the anodized 316L SS surfaces. PLGA films poured onto non-anodized 316L SS surfaces were used as control samples.

2.3   Preparation of Conductive Silk Fibroin Films with Needle-like Topographies

As a first step to obtaining the nanopore surfaces, aluminum (Al) (>99.5% Al) was cut into 1cmx4cm rectangle shaped samples. These samples were cleaned in acetone,

ethanol, and distilled water each for 10 minutes, respectively. At first, the cleaned samples were anodized with using 0.3 M oxalic acid electrolyte under 40 V and 70 V for 3 hours to obtain two different nanopore surfaces at 4°C. Afterwards, obtained oxide layer was removed by 6wt% H_3PO_4 and 1.8wt% H_2CrO_4 solution for 4 hours and 20 min at 65°C. Then, Al samples were anodized with the first anodization electrolyte, voltage, and temperature parameters for 10 min, and dried in oven.

Silk fibroin was extracted from the cocoons of *Bombyx mori*. Sericin which is the outer protein layer, was dissolved by boiling cocoons in 0.02 M Na2CO3 solution for 30 min at 80 °C. The extracted silk fibroin was dried in a fume hood for 12 h. The dried silk fibroin was dissolved in 12 M LiBr solution for 4 h at 60 °C. Afterwards, it was dialyzed against distilled water to remove Br^- and Li^+ ions for 4 days. Then, the dialyzed solution was centrifuged to remove left-over impurities for 30 min at 4 °C, followed by freezing the silk fibroin/water solution at -20 °C for 24 h. Finally, the frozen silk fibroin/water solution was lyophilized using freze dryer (Christ Alpha 2-4 LDplus, Germany). Lyophilized silk fibroin was stored at RT [24].

CNFs were treated in HNO3:H2SO4 (1:1, v:v) solution for 24 h to obtain the functional groups and then, rinsed with distilled water. Finally, they were dried inside an oven at 60 °C [61].

AAO samples were used as a mold to obtain silk fibroin and silk fibroin/CNF films with nanoscale topographies. CNF (3% of silk fibroin, 0.009 g CNF) was dissolved by ultrasonicator in 6 ml hexaafluoro-2-propanol (HFIP). Then, 0.3 g silk fibroin was dissolved in the prepared solution for 4 days. After that, the prepared solution was poured over the AAO molds, then allowed to evaporation of HFIP for 24 h at room temperature. Finally, polymer films were soaked in methanol for 3 h and then, was peeled from anodized AAO surfaces [61].

2.4   Surface Characterization

Scanning electron microscopy (SEM, FEI, NovaNano 430, Brno, The Czech Republic) was used to characterize the surface morphology of anodized 316L SS, AAO, PLGA and silk fibroin film surfaces. Prior to imaging, AAO, PLGA and silk fibroin samples were gold sputtered (Quorom SC7640 High Resolution Sputter Coater, Lewes, The UK) to obtain a conductive pathway on the sample surfaces. 20kV potential was utilized to image 316L SS, while 5kV was utilized for PLGA film surfaces.

2.5   Surface Topography Measurements

AFM (Veeco Multimode V Atomic Force Microscopy, Santa Barbara, California) was used to characterize surface topography of the samples. AFM was operated at the tapping mode and a silicone tip having 10 nm radius of curvature was used to obtain surface scans. 1 x 1 µm surface areas were scanned at 1 Hz scan rate. Scans were repeated in triplicate. AFM images were processed using Image Plus software (Peseux, Switzerland).

2.6   Chemical Analysis

PLGA and silk fibroin film surfaces were characterized with X-ray photoelectron spectroscopy (XPS, PHI, 5000 Versa Probe, Minnesota, USA) to assess metal ion transfer from 316L SS molds. In XPS analysis, monochromatic Al K$_\alpha$ X-ray source was used with an approximate vacuum pressure of 7 Pa. Scans were collected from a spot diameter of 50 µm. Films were also characterized with Fourier-Transform Infrared Spectroscopy (FTIR, Perkim Elmer 400, Waltham, Massachusetts) to determine the presence of left-over solvent. FTIR analysis was completed using attenuated total reflection configuration with 4 cm^{-1} resolution in the 4000-400 cm^{-1} range. Background

spectra were subtracted from the obtained reflectance data and an average of 4 spectra was reported for each sample.

Additional FTIR analysis was used to quantify the β-sheet structures of silk fibroin sample groups after methanol treatment. Samples were scanned in 4000- 400 cm^{-1} range with 4 cm^{-1} resolution using PerkinElmer 400 Fourier transform infrared spectrometer (Waltham, Massachusetts) using attenuated total reflection (ATR) configuration and the average of 4 spectra was reported for each sample. Background spectra were subtracted from the obtained reflectance data. To identify the secondary structure of samples, the amide I region (1595-1705 cm^{-1}) was investigated using OPUS5.0 software. Second derivative was applied to the original spectra in the amide I region with a nine-point Savitsky-Golay smoothing filter so that the number and position of bands were determined [62]. Then, the baseline was subtracted from the original band. For the curve fitting, Gaussian function was used. Areas under single bands were used to determine the fraction of the secondary structural elements [62]. Three measurements were carried out for each sample group and average values are reported.

2.7   Water Contact Angle Analysis

Hydrophobicity of the samples were characterized with sessile drop water contact angle technique using a goniometer (EasyDrop, KRÜSS GmbH, Hamburg, Germany). 3 μL ultrapure water was dropped onto PLGA and silk fibroin film surfaces and the surface contact angles were measured after 10 s. Measurements were repeated in quadruplicate for each sample.

2.8   Conductivity Analysis

For the electrical resistivity measurements, the two-point probe method was utilized (Tufan et al. 2021). An electrically conductive silver-based paste was applied to opposite sides of hydrated scaffolds. The scaffolds were secured between steel foils to maintain electrical conductivity with the silver paste during resistance measurements. The resistivity values were calculated using the measured resistance and the dimensions of the films (width, thickness and the distance between silver paste coatings). Three specimens were measured in the hydrated state in PBS for each sample and average values were reported.

2.9   Cell Culture

A mouse neuroblastoma cell line, N2a (Neuro2-a, ATCC® CCL-131™), was used to test biological performance of the PLGA and silk fibroin films *in vitro* due to the widespread use of this cell line in cytotoxicity assays.[63,64] N2a cells were cultured in Dulbecco's Modified Eagle Medium (DMEM) supplemented with 10% fetal bovine serum (FBS), 2mM L-Glutamine, and 1% penicillin/streptomycin (PS) under standard cell culture conditions (5% CO_2, 37 °C) as per established protocols [65].

2.10   Cellular Proliferation

Prior to cell culture, PLGA and silk fibroin films were cut into 6 mm diameter samples (~70 μm thick) and rinsed with sterile 1x phosphate buffer saline (PBS), 70% ethanol and 1xPBS, respectively. Afterwards, both sides of the samples were sterilized with UV light for 1 h [66].

To assess cellular proliferation, MTT assay was used. N2a cells were seeded onto the PLGA films at a density of 2×10^4 cell/cm^2. N2a cellular adhesion

and proliferation were determined at 4 h and 1, 3 and 5 days *in vitro*. At the end of the prescribed time periods, cells were treated with MTT solution (1 mg/ml, 100 μL/well) for 3 h to form formazan crystals under standard cell culture conditions (5% CO_2, 37 °C). Afterwards, formazan crystals formed on PLGA films were dissolved using 0.1 N HCl solution prepared in isopropanol (100 μL/well). The absorbance values of the solutions containing dissolved formazan were recorded using Microplate Absorbance reader (Bio-rad, Hercules, California) at 570 nm (reference wavelength-650 nm). The absorbance of the blank samples without any cells were subtracted from the obtained absorbance values. Cellular proliferation experiments were performed three times each with three replicates.

2.11   Immunofluorescence Imaging

The morphology of N2a cells was evaluated with fluorescence staining. Specifically, DAPI, anti-f-actin and anti-vinculin staining procedures were applied to observe the nuclei, cellular morphologies and focal contact formations on each sample, respectively. N2a cells were seeded at density of 1×10^4 cell/cm^2 onto the PLGA films and incubated for 72 h. At the end of 72 h, cells were fixed with 4% paraformaldehyde solution for 30 min at RT. Once 4% paraformaldehyde solutions were discarded, the fixed cells were rinsed with 1X PBS and cell membranes were permeated with 0.2% Triton X-100 for 30 min. 5% BSA in 1xPBS was used as a blocking solution. 0.5% BSA in 1xPBS was used to dilute primary and secondary antibodies. Blocking step was applied prior to and after the incorporation of primary antibody solution. For the antibody staining procedure, the permeated cells were initially incubated with anti-vinculin primary antibody (rabbit monoclonal, 1:200) for 90 min, followed by rinsing with 1xPBS. Afterwards, the cells were incubated with Alexa Flour 488 conjugated secondary antibody (goat anti-rabbit IgG, 1:1000) and rhodamine-phalloidin for 1 h. Cells were also stained with DAPI

(0.5% BSA in 1xPBS, 1:40000) 30 min to image their nuclei. Confocal microscopy (Zeiss LSM800, Germany) was used for imaging and the captured images were merged with ZEISS ZEN Imaging Software (Jena, Germany). Images were quantitatively analyzed using ImageJ (NIH, USA). Immunofluorescence staining experiments were repeated in triplicate.

2.12 SEM Imaging

In addition to immunofluorescence imaging, the morphology of the N2a cells was also evaluated with SEM imaging. Prior to SEM imaging, N2a cells were seeded at density of 1×10^4 cell/cm^2 onto the PLGA films and incubated for 24 h. At the end of 24 h, cells were fixed with 4% paraformaldehyde solution for 20 min at RT. Once paraformaldehyde solution was discarded, the fixed cells were rinsed with 1X PBS and dried gradually using 30, 70, 90 and 100% ethanol solutions, respectively. Afterwards, cells were incubated with hexamethyldisilazane for 12 h at RT for final drying. Prior to imaging, cells were sputter coated with gold (Quorom SC7640 High Resolution Sputter Coater, Lewes, UK) to obtain a conductive pathway on the samples. SEM micrographs of N2a cells were used to count number of neural cell extensions. Neurite extensions that exceeded the cell diameter in length were counted. The number of neurite extensions were normalized by dividing neurite extension number to cellular count for control, P-30 and P-80 groups (n=7) [67,68].

2.13 Protein Expression Levels with Western-Blotting

The c-fos and MAP2 protein expression levels were assessed with Western blotting to identify N2a cellular activity and microtubule production, respectively. Firstly, N2a cells were seeded onto the different films at a density of 5×10^4 cell/cm^2 and incubated for 48 h (n=3). After the incubation, cells were lysed using a buffer solution (M-PER^{TM} Mammalian Protein Extraction

Reagent) plus protease inhibitors, followed by centrifuging at 13.000 rpm for 10 min. The supernatant was assayed for protein content with Bradford assay, while 10 μg of protein from each extract were analyzed with Western blot.[69] Afterwards, the nitrocellulose membrane blots were probed with anti-c-fos (rabbit, 5% milk in phosphate buffer, 1:1000) and MAP2 (rabbit, 5% milk in phosphate buffer, 1:1000) overnight at 4 °C. Same procedure was repeated for β-actin secondary antibody (rabbit, 5% milk in phosphate buffer, 1:1500) as a loading control. Western blot signal was enhanced by chemiluminescence using goat antirabbit IgG coupled to horseradish peroxidase (5% milk in phosphate buffer, 1:10000) as the secondary antibody using a gel imaging system (BIO-RAD ChemiDoc MP Imaging System). The protein band intensities were quantified with ImageJ software (NIH, Maryland, USA). Experiments were repeated in triplicate.

2.14   Protein Adsorption on Film Surfaces Assay

Protein adsorption assay was used based on previously established protocols.[70] Briefly, 1 x 1 cm PLGA films were UV sterilized and placed separately inside the wells of tissue culture plate. DMEM medium containing 10% FBS (1 mL) was added onto each sample and incubated for 4h under standard cell culture conditions (5% CO_2, 37 °C). At the end of incubation, DMEM was discarded and each sample was rinsed with 1xPBS. Afterwards, samples were transferred to a fresh well and 300 μl protein removal buffer solution (8M urea, 0.1M TrisBase, and 0.01M DTT, adjusted pH 8.6) was added onto each sample. The samples were incubated inside the protein buffer solution for 20 min on a shaker at 40 rpm. After elution of the adsorbed proteins, the protein concentration was assayed using Bradford assay [71]. Experiments were repeated in triplicate.

2.15   Statistical Analysis

The Shapiro-Wilk test was applied to verify the normality of the results (IBM SPSS Statistics, Version 25), followed by analyzing for statistical significance using ANOVA (IBM SPSS Statistics, Version 25). Statistical significance was defined as a $p<0.05$. The values were given as mean±standard deviation (SD).

CHAPTER 3

THE NEURONAL CELL BEHAVIOURS UPON THE CELLULAR INTERACTIONS WITH NANOSCALE TOPOGRAPHIES IN DIFFERENT SCALES ON PLGA SURFACES

Neural cells interface with a variety of cell types in their natural niche which possess surface topographies in the micron and nanometer range that stimulate and have a positive impact on neural cells functions [72]. In addition, the ECM surrounding neural cells also possesses nanoscale surface arrays and has building blocks that have dimensions within nanometer regime. For instance, peripheral nerves embedded inside endonerium contain different types collagen molecules (the collagen is about 1.5 nm thickness and 300 nm long rod-shaped molecules [55]), while the basal lamina in endoneurium that surrounds Schwann cells is composed of various molecules including fibronectin (the width of fibronectin protein is approximately 3 nm [73] and heparan sulfate proteoglycan (has a protein core of 80 nm [58]) that have nanometer dimensions. Considering the nanometer size range of molecules and the concomitant nanoscale surface topography of ECM interacting with neural cells, fabrication of neural guidance channels that possess nanoscale surface topography would allow neural cells to interact with a surface that mimic their natural niche. As a matter of fact, design of implant surfaces to mimic the nanoarray size of tissues has been investigated in various biomaterial applications, including orthopedic implants where fabrication of a nanoarrayed surface topography on PLGA surfaces to mimic the inorganic component of bone tissue was observed to upregulate adhesion, proliferation and cellular functions of osteoblasts [74].

In the last decade, neural cell functions on topographical structures were investigated in detail where most studies focused on the interactions between

27

neural cells and biomaterial surfaces to have "micron" and "submicron" scale topography [75]. For instance, neural stem cells expressed longer extensions on PLGA surfaces that had 400 nm grooves compared to smooth surfaces independent of the presence of 3,4-dihydroxy-L-phenilalanin (DOPA) coating [46]. In a different study, astrocytic scar tissue formation upon the changes in nanoscale topographical array size of AAO was investigated to optimize biological interactions for neural electrode applications. The results showed that astrocyte adhesion was higher onto surfaces with small porous structures (~20 nm) compared to the ones having larger pores (~90 nm) [49]. In addition, astrocytes expressed more focal adhesions on AAO surfaces having smaller pore size [49]. Though the authors focused on the effect of surface array dimensions less than 100 nm, the material of investigation was porous aluminum oxide and astrocytes were used to investigate the efficacy of AAO for neural electrodes.

Though there are multiple studies investigating the effect of submicron (>1 µm) and micron sized topographical structures for NGC applications, studies focusing on the effect of surface array size less than 100 nm is very limited. For optimal neural regeneration, it is essential to understand neural cell functions upon their interaction with nanoscale topographies having less than 100 nm (nanoscale) lateral array size. Herein, the influence of nanoscale surface arrays fabricated on PLGA films, FDA approved material used in NGC applications, was investigated to identify an optimal nanoscale surface topography using N2a cell line (mouse neuroblastoma cells) for neural-tissue engineering applications. To understand the effect of nanoscale surface topography on neural cell functions, 316L SS surfaces having different sized nanopits were fabricated by anodization and these surfaces were used as molds to cast PLGA solution and to transfer their nanoscale surface topography onto PLGA. Scanning electron microscopy, atomic force microscopy, X-ray photoelectron spectroscopy, Fourier-Transform Infrared Spectroscopy and

28

sessile drop water contact angle measurements were used to characterize surface morphology, topography, chemistry and hydrophobicity, respectively. Cellular proliferation, morphology and activity were evaluated to understand interaction of neural cells with nanoscale PLGA surfaces.

3.1   Results

SEM micrographs of anodized 316L SS samples were given in Fig. 7. The anodization process formed nanopit structures homogenously across the 316L SS surfaces. Nanopits having two different diameters (lateral) were fabricated on 316L SS surfaces by altering the anodization conditions where anodizing at 35V for 5 min formed 32±1 nm and 50V for 6 min formed 79±1 nm sized nanopits, respectively (Fig. 7b and c). Anodized 316L SS samples were used to obtain nanoscale topographies on PLGA films via the replica molding process where 8% PLGA was poured onto the anodized 316L SS surfaces, followed by evaporation of the solvent and peeling of PLGA from the anodized 316L SS surfaces. 316L SS samples having 32±1 nm and 79±1 nm array size will be referred as 'A-30' and 'A-80 nm', respectively; and the PLGA films peeled from A-30 and A-80 will be referred as 'P-30' and 'P-80', respectively (Table 1).

Table 1. The abbreviations used for different sample types

Sample	Abbreviation for Anodized Steel	Abbreviation for PLGA Replica
Non-anodized	Control	Control
Anodized surfaces having 32±1 nm pits	A-30	P-30
Anodized surfaces having 79±1 nm pits	A-80	P-80

While the control samples molded onto non-anodized 316L SS (Fig. 7d) did not have an array of periodically repeating surface arrays, P-30 and P-80 samples displayed nanoarrays resembling the topography of anodized 316L SS surfaces (Fig. 7e and 7f). SEM images confirmed successful transfer of nanopatterns from 316L SS surfaces onto the PLGA films. Since PLGA surfaces with nanoarrays were deteriorated due to high magnification (with electron beam) during the SEM analysis, P-30 and P-80 sample surfaces were not seen as bumpy as AFM micrographs (Fig. 8). It was important to note that there was no cracking or damage during peeling of the PLGA films from the anodized 316L SS. These results were in-line with literature findings where nanoscale surface topographies were successfully transferred from AAO templates onto PLGA films [76].
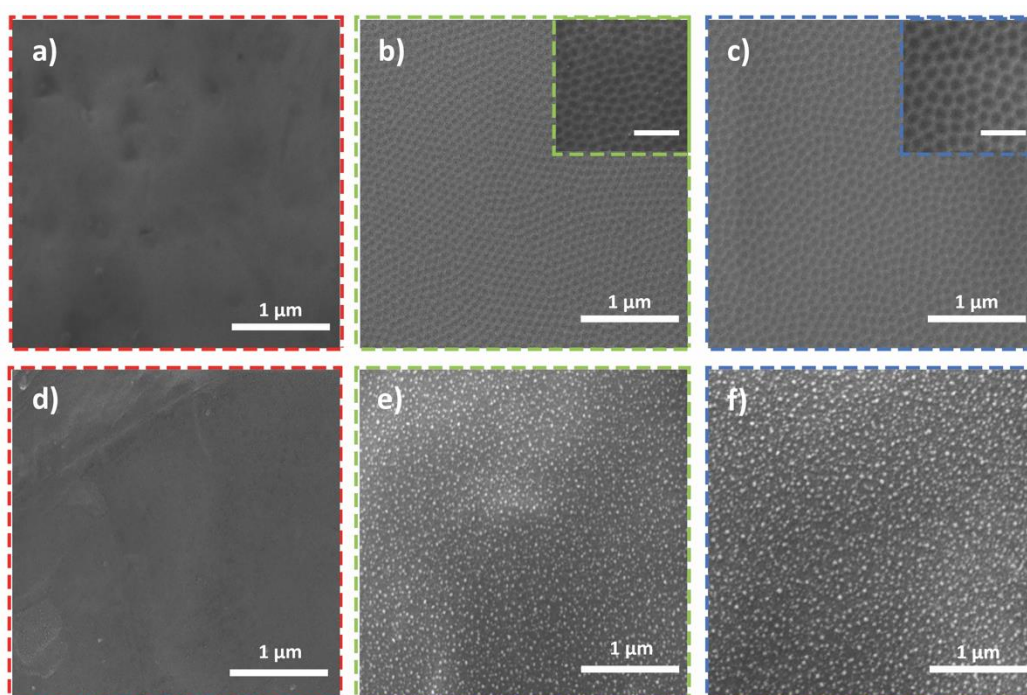
Figure 7. SEM micrographs of a) control, b) A-30 and c) A-80, d) control, e) P-30 and f) P-80 samples. The scale bars of insets are 3 μm.

2D and 3D AFM micrographs and height profiles obtained from the PLGA samples were displayed in Fig. 8. AFM micrographs further confirm

successful molding of bumpy nanoscale surface arrays onto the PLGA films. Height profile analysis provided information on the size of surface arrays on the PLGA films. The sizes of individual bumps were measured to be 29.4 ± 3.1 and 80.2 ± 3.5 nm for P-30 and P-80, respectively, and heights of individual bumps were measured to be 1.9 ± 0.1 and 4.1 ± 0.2 nm for P-30 and P-80, respectively (Fig. 8). The dimensions of nanoscale bumps on PLGA surfaces matched the array size of nanopits obtained on anodized 316L SS surfaces. The root-mean square roughness values (S_q) calculated from the scans were 1.23 ± 0.05, 1.85 ± 0.05 and 4.52 ± 0.15 nm for the control, P-30 and P-80, respectively (Table 2). The arithmetical mean square roughness values (S_a) calculated from the scans were 0.99 ± 0.04, 1.50 ± 0.03 and 3.73 ± 0.13 nm for the
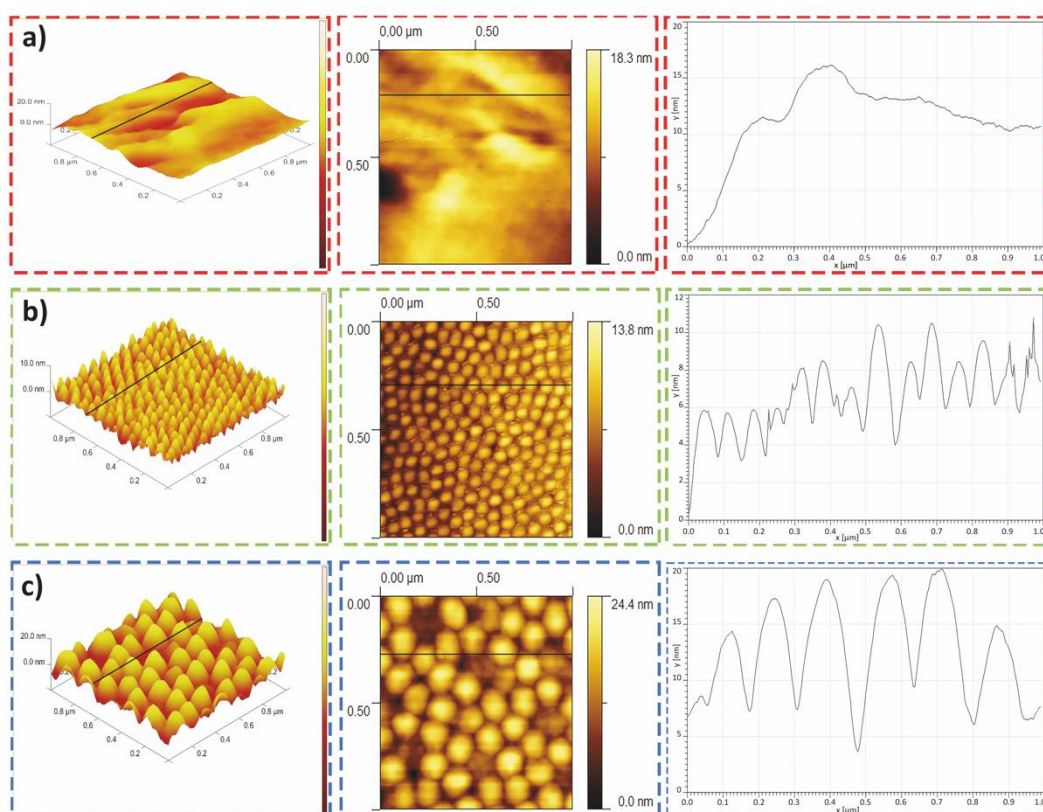
Figure 8. AFM images for a) control, b) P-30, c) P-80 samples showing 3D (left) and 2D (middle) micrographs, and height profiles (right). The thick black lines on 2D AFM micrographs indicate where height profiles were obtained on the PLGA films.

Table 2. Values for root mean square roughness, average roughness and surface area. Values are mean±SD, **$p<0.001$.

Sample	Root Mean Square Surface Roughness (S_q, nm)	Arithmetical Mean Surface Roughness (S_a, nm)	Surface Area (μm^2)
Control	1.23±0.05	0.99±0.04	1.003±0.001
P-30	1.85±0.05**	1.50±0.03**	1.016±0.001**
P-80	4.52±0.15**	3.73±0.13**	1.021±0.001**

control, P-30 and P-80, respectively (Table 2). The S_q and S_a values for P-30 and P-80 were both higher compared to the control samples ($p<0.001$). The obtained differences in surface roughness values were expected and in-line with the principles of anodization. Specifically, during anodization process 316L SS surfaces were polished to a near mirror finish and all surface extremities, including grain boundaries, were removed from the anodized surfaces. Having this said, aside from polishing and smoothing out large surface asperities, anodization process also formed nanopit arrays on 316L SS surfaces. Upon molding of PLGA onto the anodized 316L surfaces, arrays of nanoscale bumps formed on PLGA, which led to an increase in S_q and S_a values. In this study, surface areas were measured to be 1.003±0.001, 1.016±0.001 and 1.021±0.001 μm^2 for control, P-30 and P-80 samples, respectively. Though the increase in surface areas for P-30 and P- 80 were minor, they were found to be statistically significant compared to the control ($p<0.001$). During anodization process, polishing of surface asperities and formation of nanopits on 316L SS were taking place simultaneously, where the former one was decreasing, yet, the latter one was increasing the total surface area. PLGA films having nanoscale surface topographies were

characterized with XPS and FTIR for chemical analysis (Fig. 9a and Fig. 10). It was important to note that PLGA films peeled from the anodized 316L SS surfaces did not express Fe, Cr, Ni, and Mo peaks in their XPS spectra indicating that the oxide layer did not delaminate from the anodized 316L SS surfaces and stick to PLGA films during replica molding process [77]. Interestingly, XPS results revealed presence of trace silicon on PLGA films. Specifically, 3.2, 2.2 and 1.5% silicon were observed for control, P-30 and P-80 surfaces. It can be speculated that the use of glassware during specimen fabrication led to silicon contamination on the surfaces. FTIR spectra of the PLGA samples revealed characteristic C-H (2850 cm^{-1}), C=O (1747 cm^{-1}), CH$_3$ (1383 cm^{-1}) and CH$_2$ (750 cm^{-1}) absorption bands that belong to PLGA
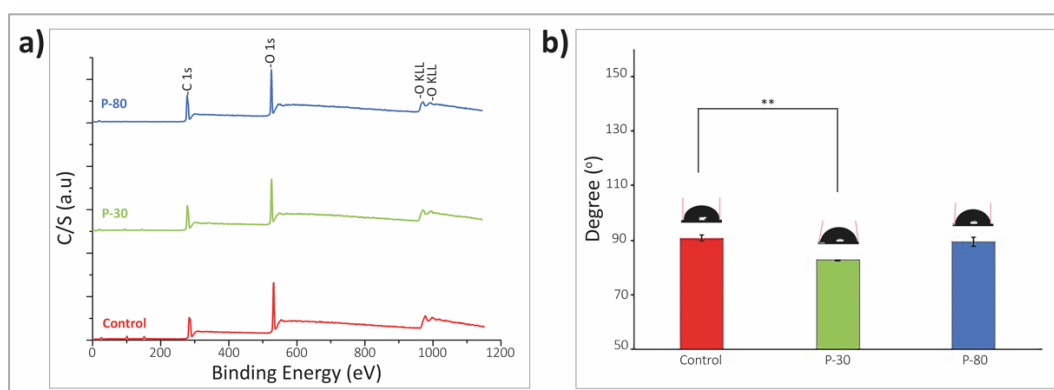
Figure 9. a) XPS and b) water contact angles for PLGA samples. Values are mean±SD, **$p<0.001$.
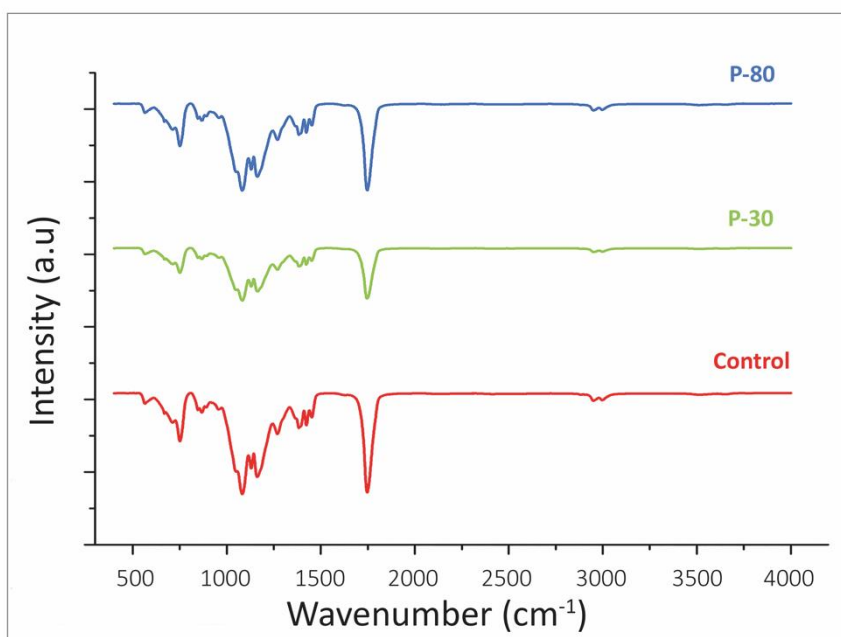
Figure 10. The chemical bond analysis results (FTIR) for all PLGA groups. It was observed that there is no difference between control, P-30 and P-80 samples.

film surfaces [78,79]. It was important to note there were no Cl peaks in the XPS or FTIR spectra of PLGA that would indicate the presence of left-over chloroform in this study. Chloroform was used to dissolve the PLGA polymer during replica molding and our results confirm successful removal of chloroform from the PLGA film surfaces.

Sessile drop water contact angles for the control, P-30 and P-80 groups were measured as 90.8°±1.1°, 82.7°±0.2°, and 89.4°±1.7°, respectively (Fig. 9b). P-30 samples expressed lower water contact angle compared to the control samples ($p<0.001$) and exhibited hydrophilic characteristics ($\theta<90°$). However, there were no statistical difference between control and P-80 samples. The small decrease in the water contact angle of P-30 could be attributed to the presence of silicon on the surfaces, which was stated in the results for XPS analysis.
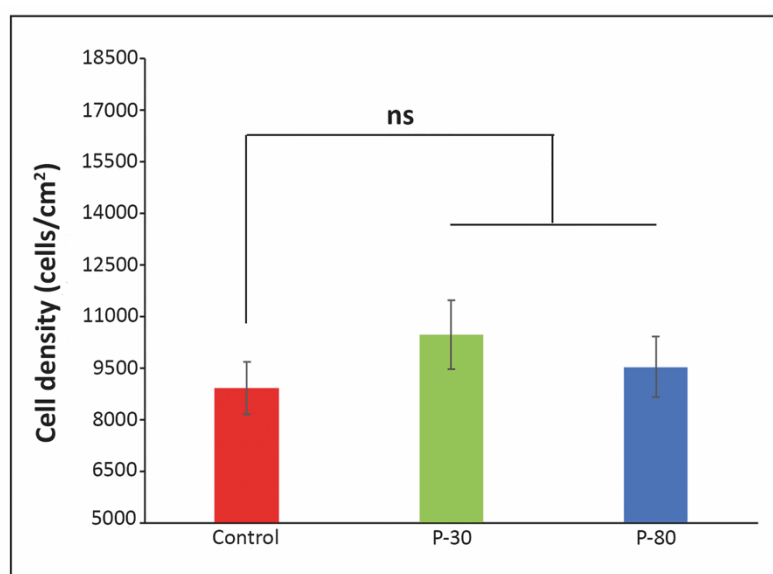
Figure 11. Cellular density (adhesion) results of N2a cells at 4 h on different PLGA film groups.
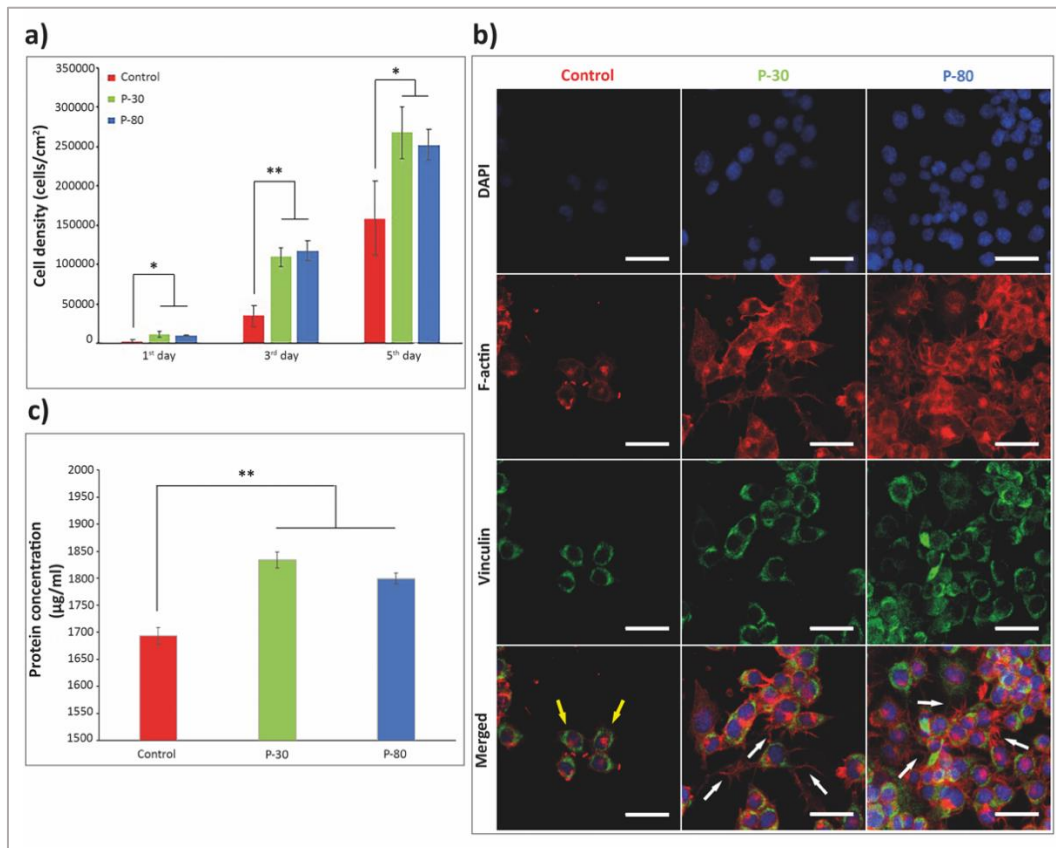
Figure 12. a) N2a proliferation on control, P-30 and P-80 samples up to 5 days in vitro. Values are mean±SD (n = 3), *$p<0.05$, **$p<0.01$. b) The N2a cells stained with DAPI for nucleus (blue fluorescence, 1st row), phalloidin for f-actin (red fluorescence, 2nd row) and Alexa-Fluor 488 for vinculin (green fluorescence, 3rd row) on control, P-30 and P-80 samples after 72 h incubation. Bottom row shows the merged images. Scale bars are 20 μm. c) Protein adsorption results for control, P-30 and P-80 samples.

N2a cellular density at 4 h (cellular adhesion) and 1st, 3rd and 5th day time points (cellular proliferation) were shown in Fig. 11 and Fig. 12a. N2a cell densities did not reveal any significant difference between the samples at 4 h, indicating that cellular adhesion was similar onto all surfaces independent of the surface topography. Having this said, N2a cells proliferated on all samples and cellular densities on control, P-30 and P-80 increased up to 5 days of culture. At the 1st day *in vitro*, P-30 and P-80 samples had higher cellular density compared to the control samples ($p<0.05$). At the 3rd day, N2a cellular densities were again higher on P-30 and P-80

compared to the control samples ($p<0.01$). However, the differences in cellular densities between the nanoscale samples and the control sample decreased at the 5th day of culture ($p<0.05$). This was probably due to N2a cells reaching confluency on P-30 and P-80 samples that slowed down their proliferation rate (Fig. 12a). On the other hand, cellular densities on P-30 and P-80 were similar at all investigated time points. These results showed that the increase in the cellular density between control and nanoscale PLGA groups were due to increased cellular proliferation.

We explored focal adhesions which are cellular sensing machinery of the cells. Focal adhesions are large macromolecular networks that facilitate communication between cells and their ECM, and vinculin is a part of focal adhesion macromolecule network. Thus, the recruitment of vinculin protein was investigated by immunofluorescence staining to visualize adhesion profile of N2a cells. N2a cells cultured on control, P-30 and P-80 surfaces were stained for their nuclei (blue), f-actin filaments (red), vinculin protein (green) and the images were displayed in Fig. 12b. The merged immunofluorescence images (bottom row) qualitatively revealed that nanoscale PLGA films had higher number of neural extensions (white arrows) and each of these neural extensions were longer than the control group (yellow arrows). Additionally, focal adhesions were observed to be distributed peripherally in all investigated samples. Cellular morphologies were also investigated using SEM and the captured images revealed that N2a cells expressed more neural extensions on P-30 and P-80 than the control samples ($p<0.01$) (Fig. 13a, b and c). In fact, N2a cells had 0.38±0.06, 1.29±0.55 and 1.83±0.76 neurite extensions per cell for the control P-30 and P-80 samples, respectively. However, no statistical significance in the number of neurite extensions per cell was detected between the P-30 and P-80 (Fig. 13d). Clearly, cell-material interactions, which enhanced N2a proliferation and triggered the formation of focal adhesions and neural extensions, occurred at a higher extent on nanoscale PLGA surfaces compared to the control surface.
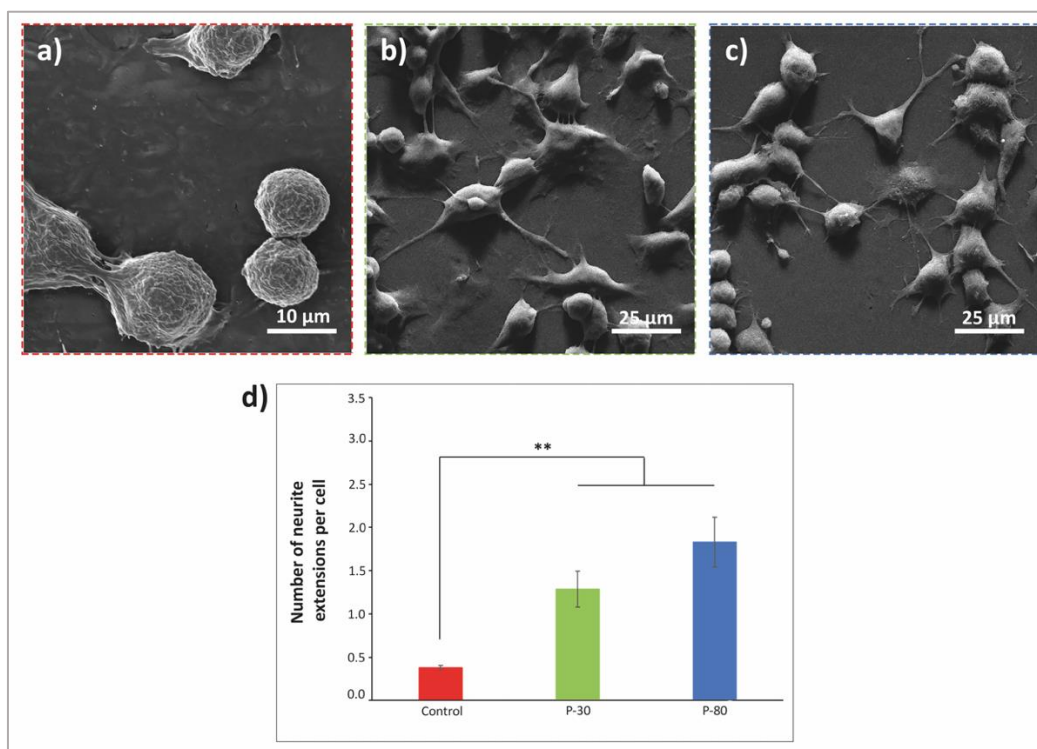
Figure 13. SEM images of N2a cells on a) control, b) P-30 and c) P-80 samples. d) Number of neurite extension per cell for the control, P-30 and P-80 samples. The values are mean±SD, n=7, **$p<0.01$.

It is well-known that cells interact with proteins adsorbed onto material surface, rather than directly interacting with the material itself [80]. In Fig. 12c, it was observed that protein adsorption was significantly higher for P-30 and P-80 compared to control where 1693.3±27.2, 1833.9±25.8 and 1799.1±18 μg/ml were found for the control, P-30 and P-80 samples, respectively. As a result of the protein adsorption profiles, N2a cells were adhering, proliferating and expressing more neural extension on P-30 and P-80 compared to control surfaces. In fact, these results were in-line with literature findings, where increase in density and functions of different cell types were associated with increased total protein adsorption, while increased protein adsorption was correlated with the increased surface roughness [80–82]. For instance, TiO$_2$ surfaces having nanoleave morphology enhanced total serum protein

adsorption onto its surfaces, which contributed to the increased endothelial cell viability compared to polished titanium. In addition, the dimensions of the nano-pores fabricated on poly(L-lactic acid) microfibers were found to enhance total protein adsorption, which was further correlated with cytocompatibility of these scaffolds to support vascular smooth muscle cell adhesion, proliferation and expression of the vascular matrix proteins (elastin and collagen) [83,84].
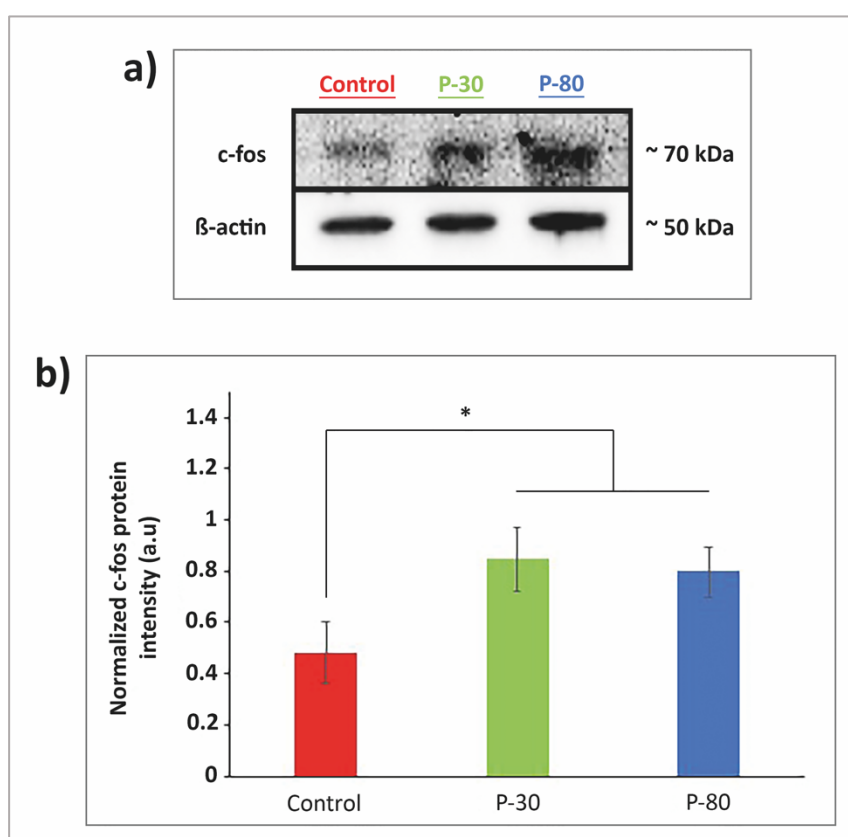
Figure 14. a) Immunoblot images of control, P-30 and P-80 samples using anti-c-fos and anti-β-actin, b) Western-blot analysis of c-fos protein in N2a cells cultured on control, P-30 and P-80 samples. The values are mean±SD, n=3, *$p<0.05$.

C-fos protein has a key role in mitogen-activated protein kinase (MAPK) cascade mechanism, which maintains and controls the cellular proliferation, differentiation, and migration, and its expression is vital for firing neurons [85].

The c-fos expression levels were determined by Western blot to assess N2a cellular activity. As seen in Fig. 14, the normalized intensity values for c-fos protein expressions were 0.48±0.12, 0.85±0.12 and 0.80±0.10 (a.u) for the control, P-30 and P-80 samples, respectively. Western blot results showed that cells cultured on P-30 and P-80 films had higher c-fos protein expression compared to the control samples (Fig. 14, $p<0.05$). These results also confirmed that P-30 and P-80 enhanced N2a cellular functions compared to control samples.

3.2   Discussion

In NGC applications, surface modifications to induce topographical arrays have an important role in directing growth of axons between the damaged proximal and distal stumps. In our study, nanoscale arrays having 30 nm and 80 nm lateral sizes were formed on PLGA films, which is a frequently used material in NGC applications, and the effect of surface nanoscale topography on N2a cellular functions were investigated. The differences observed in N2a behavior on P-30 and P-80 films for the enhanced cellular functions suggested that cells sensed the subtle changes in the surface nanoscale topography and reacted with a complex physiochemical response. This was in-line with previous findings where changes in nanoscale surface topography altered cellular functions. For instance, altered array size on anodized surfaces independently allowed either augmented human mesenchymal stem cell adhesion when array size was ~30 nm or specific differentiation into osteoblasts when array size was ~70-100 nm [39]. In another study, human mesenchymal stem cells expressed well-spread cellular morphology with large focal adhesions on 15 and 55 nm high nanopillar surfaces compared to 100 nm high nanopillar surfaces [86]. Along the same line, electrospun fiber scaffolds with nanopits were shown to enhance interleukin-12 expression for M1

polarized macrophages compared to fibers having divots [87,88]. In this study, N2a cells had higher densities, higher number of neural extensions and up-regulated c-fos expression on P-30 and P-80 compared to the control samples. The reason for the enhanced N2a functions could be explained with changes in surface topography of PLGA films, where P-80 and P-30 surfaces had an array of nanoscale surface features which led to higher rms roughness values compared to the control samples. In fact, on gold surfaces having similar roughness values to the ones investigated in this study, neuronal cells had the lowest necrosis rate, expressed axonal outgrowth and functional cytoskeletal orientation, while increase in roughness to 80-100 nm led to disorganized focal adhesion complexes [89]. It was clear that N2a cells sensed the nanoscale topography introduced onto P-30 and P-80 surfaces and responded by enhancing their proliferation and functions. Having this said, the lack of surface asperities removed from 316L SS during anodization, yet present on the control samples, could have contributed to the promotion of cellular functions for P-30 and P-80 samples. In addition to the effect of surface topography, the increased hydrophilicity was known to dictate neural cell adhesion, proliferation and functions and focal adhesion expression [49]. Since P-30 was hydrophilic compared to the control sample, perhaps, increased hydrophilicity of P-30 could have a minor contribution for the observed differences in N2a cellular functions [90,91]. However, the changes in hydrophilicity could not account for the increased cellular function on P-80.

Since the total amount of proteins adsorbed onto the PLGA films increased upon surface modification, it could be speculated that the adsorption of cell adhesive serum proteins, *i.e.* fibronectin and laminin, which were demonstrated to control adhesion, proliferation and functions of anchorage dependent cells also increased [92]. In fact, the surface concentration and bioavailability of fibronectin and collagen type IV were shown to enhance on nanoscale PLGA compared to its conventional counterpart [60,93]. It could be speculated that enhanced concentration of cell adhesive serum proteins on P-

30 and P-80 surfaces could have contributed to the observed changes in the cellular functions of N2a cells.

To sum up, our results indicated that nanoscale topographical arrays having lateral dimensions less than 100 nm may provide positive impacts on the proliferation and functions of neurons. Thus, fabrication of nanoscale surface topographies should be investigated further for the next generation NGCs for PNS injuries.

CHAPTER 4

THE NEURONAL CELL BEHAVIOURS UPON THE CELLULAR INTERACTIONS WITH NANOSCALE TOPOGRAPHIES IN DIFFERENT SCALES ON CONDUCTIVE SILK FIBROIN SURFACES

PNS injuries are a common condition with various challenges to patients life, ranging from mild discomforts to life-long impairment. The recent analyses showed that the rate of cases due to PNS damages are 1/1000 per year. Additionally, in the United States alone, annual patient care costs were reported as around $150 billion [94]. Autografts as gold standart, allografts and xenografts are mainly treatment methods for PNI regeneration [2]. Since there are many risks as causing immune response in patient biological system, having limited availability from donor tissue and lack sufficient number of donors etc., NGCs were alternatively developed for neural tissue engineering applications. NGCs are tube or canal structures that are placed between the distal end of the damaged nerve and the proximal end, and support the damaged axon structure to be correctly directed and extended between the two ends to allow the regeneration process. NGCs should have properties to support the recovery of damaged nerve structure such as supporting neural cell adhesion, proliferation and cell function to heal properly, being conductive, to ensure the rapid and accurate orientation of neural cell extensions and having similar structures as the biological environment ECM [95].

The results of nerve regeneration may vary depending on the characteristics of that NGCs, therefore, they should have characteristic physical, chemical and electrical properties. There are various studies in the literature to provide conductivity and similar features to NGCs. One of the areas used to obtain these features for NGCs is the nanotechnology field, which refers to the use of physical and chemical changes in the material for new or different applications by controlling the material sizes

below 100 nm which are also called nanomaterials. While the functionality of neural cells can be maintained by providing conductivity to the material, the biological environment of the neural cells and axons is mimicked and the axons in the regeneration process can be linearly directed by providing the hierarchical structure with micron and nano-dimensional structures.

There are several studies in the literature about the effects of nanotopographical structures on the neural cells behaviour. Previous studies have concluded that the physical properties of the material surface can have favorable effects on neuronal cells. However, there are limited studies that systematic nanotopographical structures on the material surface and conductivity may have impact on cell behaviour. In this thesis, we hypothesized that understanding the effects of the usage of silk material making conductive which is more biocompatible than PLGA and obtain systematic nanotopographical structures on these surfaces on N2a cells. Moreover, new data was conveyed by providing comparison with obtained nanostructured PLGA films. According to this, first, CNF was added as a secondary phase in order to provide conductivity to the silk material commonly used in tissue engineering. Then, two different nano and sub-micron level nanotopographies, 50 nm and 125 nm, where the neural cells was adhered and positioned, were fabricated on the silk-CNF film surfaces to obtain hybrid silk-CNF film surfaces. When these surfaces were obtained, their effects on the neural cells such as proliferation, viability, neural cell functions and morphologies were investigated.

4.1   Results

SEM micrographs of AAO samples were shown that the anodization process formed nanoporous structures homogenously across the AAO surfaces (Fig. 15). Nanopores having two different diameters (lateral) were fabricated on AAO surfaces by altering the anodization conditions where anodizing at 40V with three steps formed 47±6 nm and 50V with three steps formed 122±17 nm sized nanopores, respectively (Fig. 15a and b). AAO samples were used to obtain needle-like topographies on silk fibroin

and silk fibroin-CNF films via the replica molding process where silk fibroin and silk fibroin-CNF was poured onto the AAO surfaces, followed by evaporation of the solvent and peeling of the silk fibroin films from the AAO surfaces. AAO samples having 47±6 nm and 122±17 nm array size were referred as 'Al-50' and 'Al-125 nm', respectively; and the silk fibroin films peeled from Al-50 and Al-125 were referred as 'S-50' and 'S-125' and the silk fibroin-CNF films peeled from Al-50 and Al-125 were referred as 'SC-50' and 'SC-125', respectively as depicted in Table 3.

Table 3. The abbreviations used for different sample types.

Sample	Anodized Aluminum	Silk Replica	Silk/CNF Replica
Glass surface	-	S-smooth	SC-smooth
Anodized surfaces having 48±6.6 nm pores	Al-50	S-50	SC-50
Anodized surfaces having 123±17.6 nm pores	Al-125	S-125	SC-125

Table 4. Values for root mean square roughness, average roughness and surface area. Values are mean±SD, **$p < 0.001$.

Sample	Root Mean Square Surface Roughness (S_q, nm)	Arithmetical Mean Surface Roughness (S_a, nm)	Surface Area (μm^2)
S-smooth	2.54±0.07	2.02±0.06	1.03±0.01
SC-smooth	2.21±0.17**	1.69±0.14**	1.01±0.00
S-50	12.33±1.25**	9.71±0.91**	1.16±0.02**
SC-50	10.83±0.32**	8.52±0.22**	1.17±0.02**
S-125	13.21±3.12**	10.24±2.45**	1.08±0.03
SC-125	14.36±1.84**	11.63±1.5**	1.15±0.01**

The control samples (smooth surfaces; S-smooth and SC-smooth) molded onto glass surface (Fig. 16a and b) did not have an array of periodically repeating surface arrays, remaining samples (S-50, SC-50, S-125 and SC-125) displayed needle-like topographies resembling the topography of AAO surfaces (Fig. 16c, d, e and f). SEM images confirmed successful transfer of nano-patterns from AAO surfaces onto the silk fibroin films. It was important to note that there was no cracking or damage during peeling of the silk fibroin films from the AAO. These results were in-line with literature findings where nanoscale surface topographies were successfully transferred from AAO templates onto silk fibroin films as PLGA films results [76].
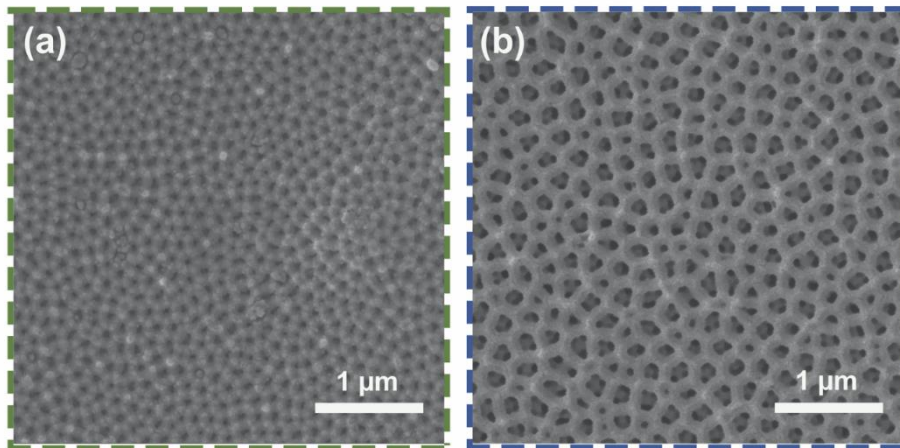
Figure 15. SEM micrographs of a) Al-50 and b) Al-125 AAO samples. The scale bars of insets are 1 μm.
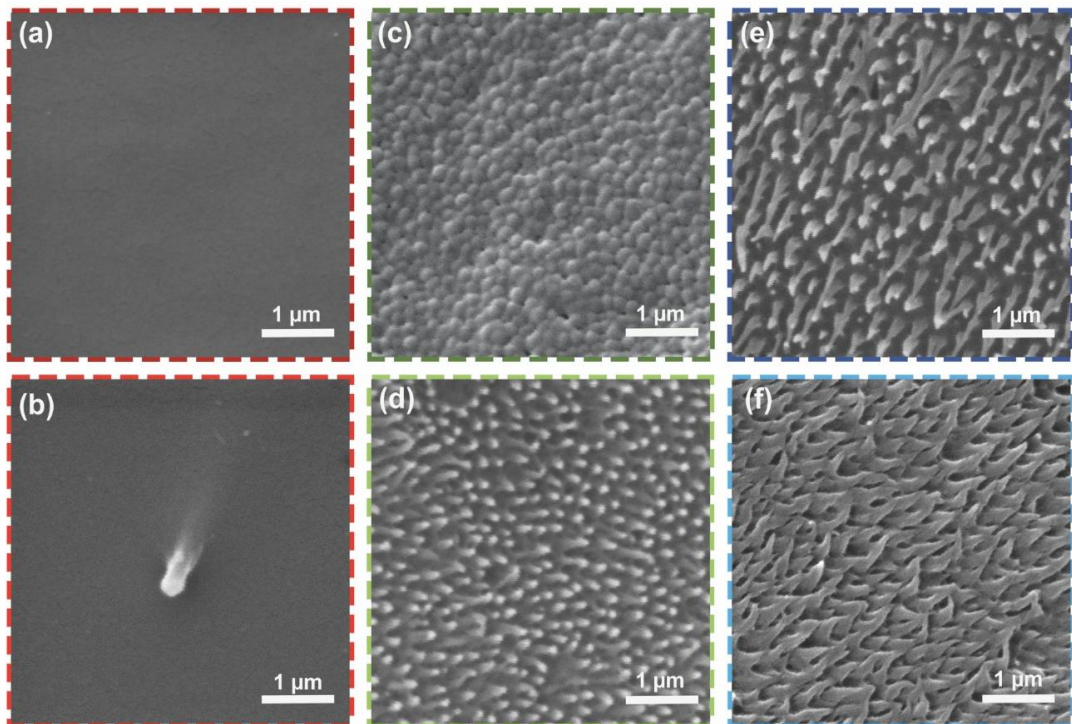
Figure 16. SEM micrographs of a) S-smooth, b) SC-smooth, c) S-50, d) SC-50, e) S-125 and f) SC-125 samples. The scale bars of insets are 1 μm.

47

2D and 3D AFM micrographs and height profiles obtained from the silk fibroin and silk fibroin-CNF samples were depicted in Fig. 17. AFM micrographs further confirm successful molding of needle-like surface arrays onto the silk fibroin films. The root-mean square roughness values (S_q) calculated from the scans were 2.54±0.07, 2.21±0.17, 12.33±1.25, 10.83±0.32, 13.21±3.12 and 14.36±1.84 nm for the S-smooth, SC-smooth, S-50, SC-50, S-125 and SC-125, respectively. The arithmetical mean square roughness values (S_a) calculated from the scans were 2.02±0.06, 1.69±0.14, 9.71±0.91, 8.52±0.22, 10.24±2.45 and 11.63±1.5 nm for the S-smooth, SC-smooth, S-50, SC-50, S-125 and SC-125, respectively (Table 4). The S_q and S_a values for SC-smooth, S-50, SC-50, S-125 and SC-125 were both higher compared to the control samples (**$p<0.001$). The obtained differences in surface roughness values were expected and in-line with the principles of anodization. Specifically, during anodization process and removing oxide layer, aluminum surfaces were polished to a near mirror finish and all surface extremities, including grain boundaries, were removed from the anodized surfaces. Aside from polishing and smoothing out large surface asperities, anodization process also formed nanopore arrays on aluminum surfaces. Upon molding of silk fibroin onto the AAO surfaces, arrays of needle-like topographies formed on silk fibroin films, which led to an increase in S_q and S_a values. In this study, surface areas were measured to be 1.03±0.01, 1.01±0.00, 1.16±0.02, 1.17±0.02, 1.08±0.03 and 1.15±0.01 μm^2 for S-smooth, SC-smooth, S-50, SC-50, S-125 and SC-125, respectively. Though the increase in surface areas for S-50, SC-50 and SC-125 were minor, they were found to be statistically significant compared to the S-smooth (**$p<0.001$). During anodization and removal of oxide layer processes, polishing of surface asperities and formation of nanopores on aluminum surfaces were taking place simultaneously, where the former one was decreasing, yet, the latter one was increasing the total surface area.
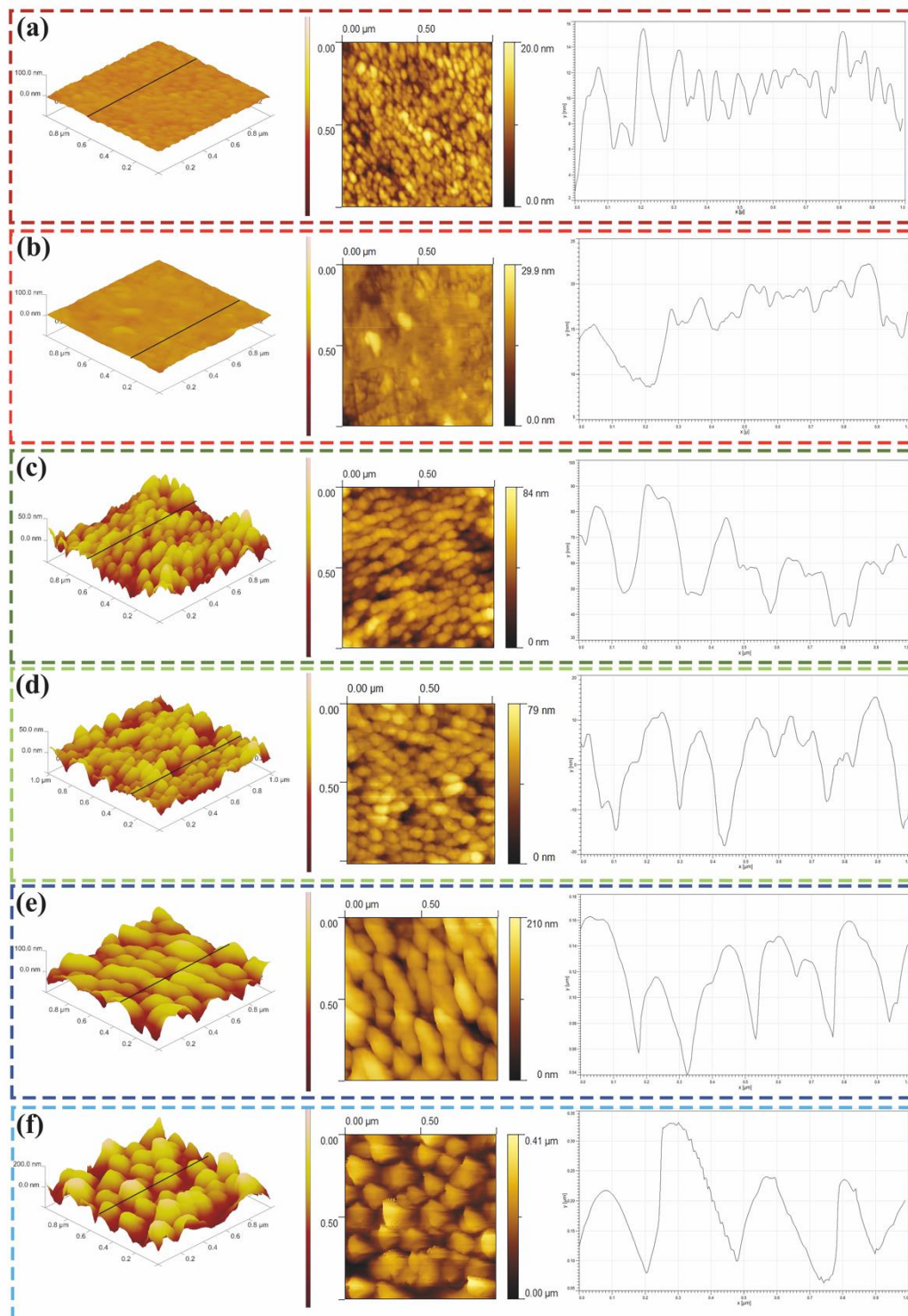
Figure 17. AFM images of a) S-smooth, b) SC-smooth, c) S-50, d) SC-50, e) S-125 and f) SC-125 samples showing 3D (left) and 2D (middle) micrographs, and height profiles (right).

49

FTIR spectra of the S-50, SC-50, S-125 and SC-125 groups revealed characteristic amide I (1235 cm-1), amide II (1517 cm-1) and amide III (1230 cm-1) absorption bands that belong to silk film surfaces (Fig. 18a) (Movasaghi et al. 2008). It was also observed that β-sheet crystallites were formed in all silk fibroin and silk fibroin-CNF groups. The percentage of β-sheet crystallites, random coil and α-helix, and also turns and side chains structures were similar in all sample groups and there was no statistically difference between any groups (Fig. 18b).
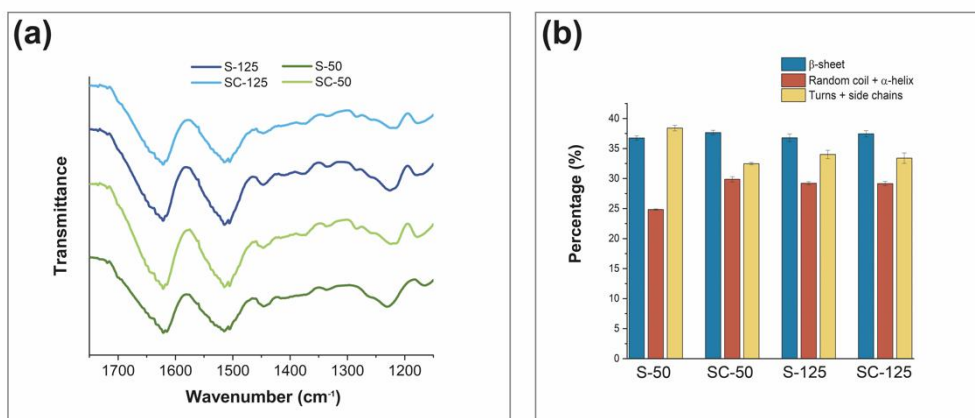
Figure 18. The chemical bond analysis using FTIR. a) S-50, SC-50, S-125 and SC-125 sample groups. b) Percentage of the β-sheet, random coil + α-helix and turns + side chains for S-50, SC-50, S-125 and SC-125 sample groups. There was no difference between silk and silk/CNF films for both topographies.

Sessile drop water contact angles for S-smooth, SC-smooth, S-50, SC-50, S-125 and SC-125 groups were measured as 103.88°±3.33°, 86.80°±2.04°, 88.60°±2.2°, 94.93°±2.76°, 94.04°±1.29° and 109.24°±3.47°, respectively (Fig. 19a). If the contact angle of surface is greater than 90°, it means that the surface is hydrophobic while if the contact angle of surface is lower than 90°, it means that the surface is hydrophilic. Based on that, SC-smooth and S-50 consisted of hydrophilic properties while S-smooth, SC-50, S-125 and SC-125 surfaces had hydrophobic properties. SC-125 samples expressed statistically

50

significant higher water contact angle compared to S-smooth samples (**$p<0.001$) and exhibited hydrophobic characteristics ($\theta>90^{\circ}$). On the other hand, SC-50 and S-125 samples expressed statistically significant lower water contact angle compared to S-smooth samples (**$p<0.001$), and they have hydrophilic characteristics ($\theta>90^{\circ}$).
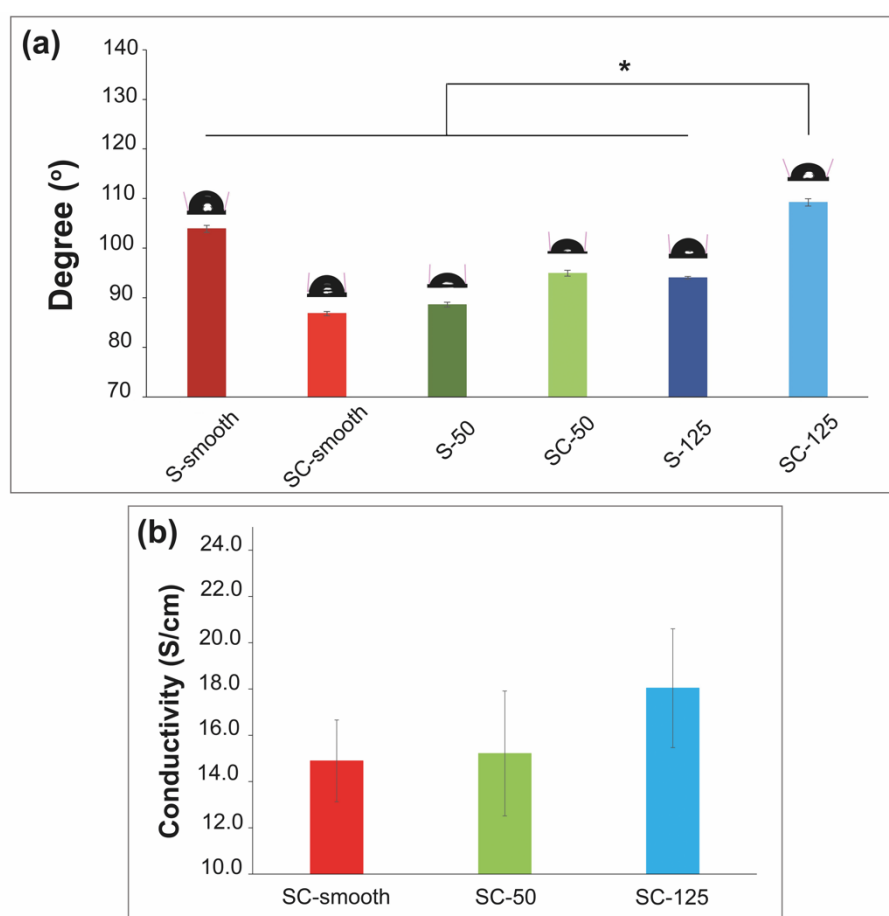
Figure 19. a) Water contact angles for all sample groups. SC-125 samples expressed statistically significant higher water contact angle compared to all other groups. b) Conductivity results for SC-smooth, SC-50 and SC-125 sample groups. There was no significant difference between all groups for conductivity results. Values are mean±SD, *$p<0.05$.
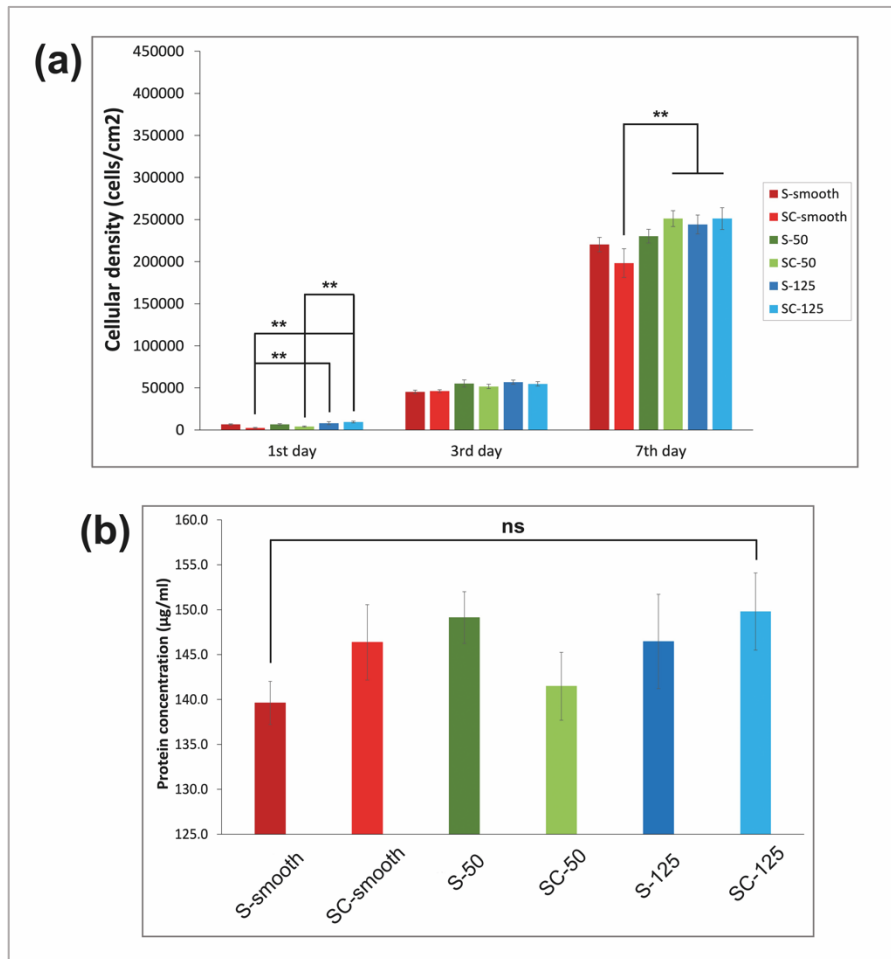
Figure 20. The results of _in vitro_ studies with all sample groups. a) N2a proliferation on all silk fibroin and silk fibroin-CNF samples up to 7 days in vitro and b) the concentration of protein adsorption results. Values are mean±SD (n = 3), **$p<0.01$. There was no statistically significant difference between groups for protein adsorption results.
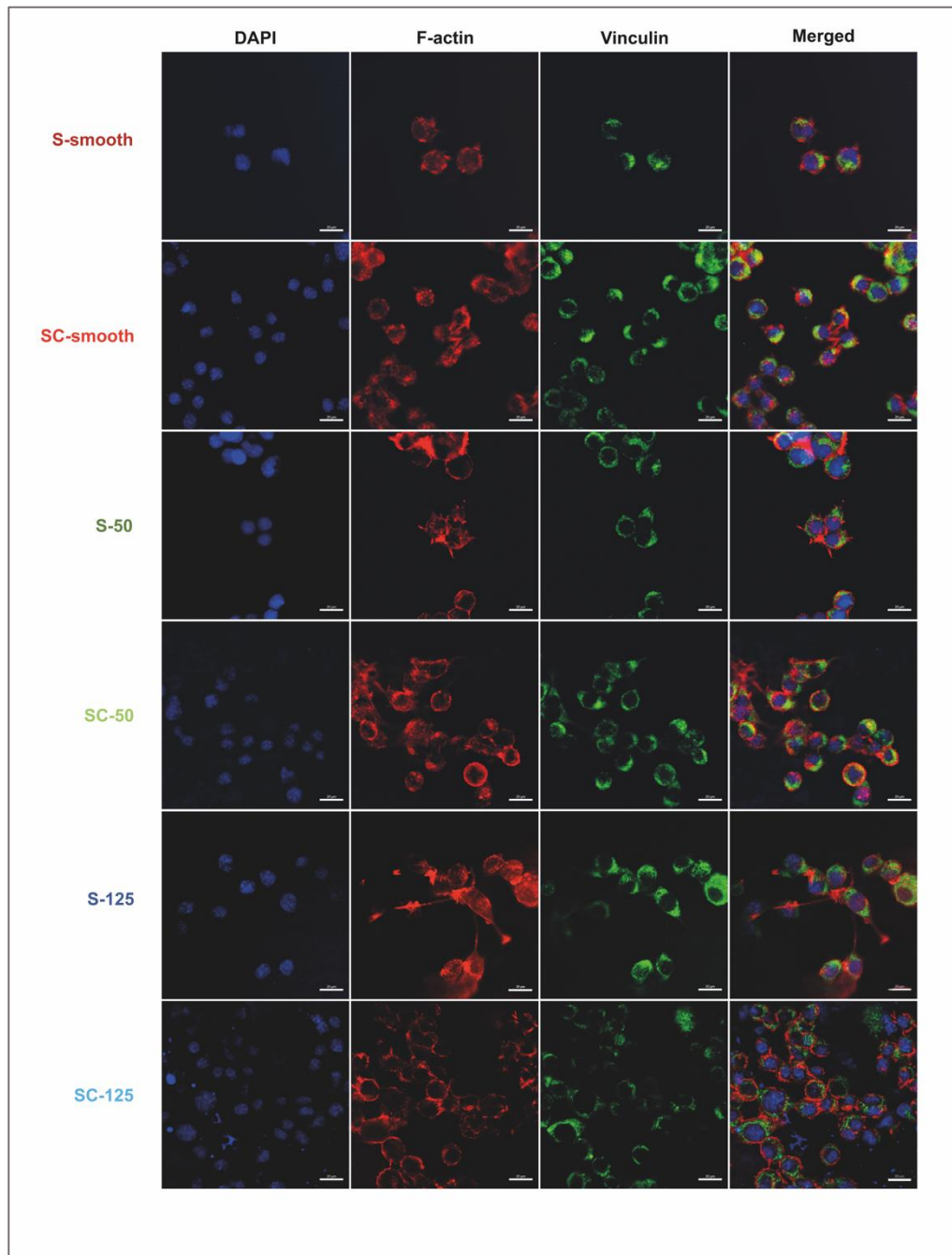
Figure 21. Confocal microscopy images of N2a cells. 1st column is the N2a cells stained with DAPI for nucleus (blue fluorescence), 2nd column is phalloidin for f-actin (red fluorescence) and 3rd column Alexa-Fluor 488 for vinculin (green fluorescence,) on S-smooth, SC-smooth, S-50, SC-50, S-125 and SC-125 samples after 72 h incubation. The last right row shows the merged images. Scale bars are 20 μm. The merged immunofluorescence images qualitatively revealed that the needle-like topographical silk fibroin and also silk fibroin-CNF films had higher number of neural extensions.

Electrical conductivities were measured in the hydrated state in PBS and the results were found as 14.89±3.1, 15.22±4.7 and 18.04±4.4 S/cm-1 for SC-smooth, SC-50 and SC-125 groups, respectively (Fig. 19b). There was no statistically significant difference. Additionally, there was no conductivity for only silk fibroin groups, since they did not have any CNF.

N2a cellular proliferation at 1st, 3rd and 7th day time points and protein adsorption results were shown in Fig. 20a and Fig. 20b, respectively. Protein adsorption did not show any statistically significant difference between the samples at 4 h (Fig. 20b). These results indicating that protein adsorption on the surfaces were similar onto all surfaces independent of the surface topography at 4 h. N2a cells proliferated on all samples and cellular densities on S-smooth, SC-smooth, S-50, SC-50, S-125 and SC-125 increased up to 7 days of culture. At the 1st day in vitro, SC-125 samples had higher cellular density compared to both SC-smooth and SC-50 samples (**$p<0.001$) and S-125 samples had higher cellular density compared to SC-smooth samples (**$p<0.001$). At the 3rd day, N2a cell densities were similar by means of any group with no statistically significant difference. At the 7th day, SC-125 and SC-50 samples had higher cellular density compared to SC-smooth samples (**$p<0.001$) (Fig. 20a). On the other hand, cellular densities on S-50, SC-50, S-125 and SC-125 were similar at all investigated time points. These results showed that the increase in the cellular density between the control and the needle-like topographical silk-fibroin groups were due to increased cellular proliferation.

Investigation of focal adhesions, which are cellular sensing machinery of the cells, were conducted. Vinculin as a part of focal adhesion macromolecule network were utilized to visualize adhesion profile of N2a cells by immunofluorescence staining. Immunofluorescence images of N2a cells that cultured on S-smooth, SC-smooth, S-50, SC-50, S-125 and SC-125 surfaces show their nuclei (blue), f-actin filaments (red) and vinculin (green) (Fig. 21).

The merged immunofluorescence images qualitatively revealed that the needle-like topographical silk fibroin and also silk fibroin-CNF films had higher number of neural extensions and these data confirmed by SEM images of N2a cells (Fig. 23). Additionally, each of these neural extensions were
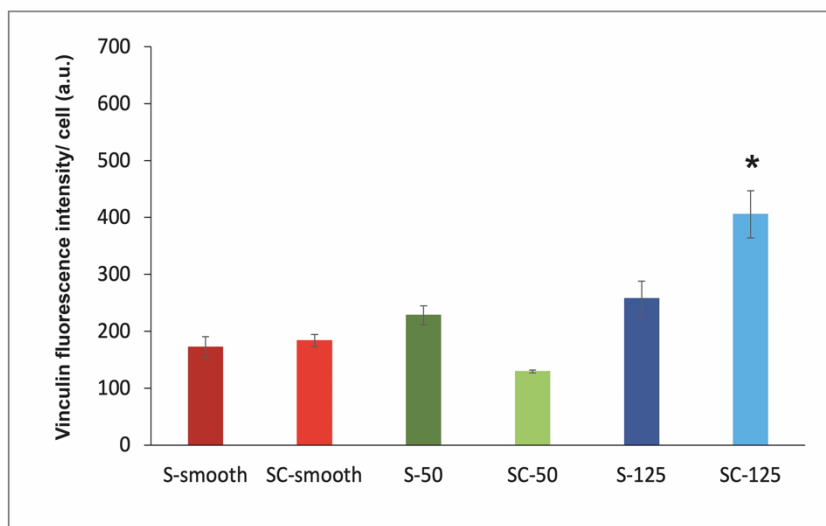
Figure 22. Vinculin fluorescence intensity levels for all silk fibroin and silk fibroin-CNF samples. The intensity for SC-125 groups were significantly higher than the other groups. Values are mean±SD (n = 3), *p<0.05.

longer than the smooth silk fibroin groups. Focal adhesions were observed to be distributed peripherally in all investigated samples.

Vinculin fluorescence intensity were analyzed by using ImageJ (Fig. 22) indicated that vinculin intensity for SC-125 groups were significantly higher than the other groups. In addition, the intensity for S-125 were statistically significant higher than SC-50 samples. In fact, N2a cells had 172.1±32, 183.7±18, 228.1±29, 129.4±4, 257.4±53 and 405.4±72 vinculin intensity (a.u.) per cell number for S-smooth, SC-smooth, S-50, SC-50, S-125 and SC-125, respectively. Data indicates that higher needle-like topographical structures which are S-125 and SC-125 groups enabled more vinculin protein expressions for N2a cells. Cellular morphologies were also investigated using SEM and the captured images revealed that N2a cells expressed more neural

extensions and these neural extensions were longer on S-50, SC-50, S-125 and SC-125 than the smooth samples (Fig. 23). Among these results, the number of neural extensions per cells for SC-125 was found statistically significant compared the other groups (**$p<0.001$) (Fig. 23f). In fact, N2a cells had 0.10 ± 0.04, 0.26 ± 0.08, 0.42 ± 0.10, 0.61 ± 0.11, 0.87 ± 0.14 and 3.11 ± 0.71 neurite extensions per cell for S-smooth, SC-smooth, S-50, SC-50, S-125 and SC-125 samples, respectively. Evidently, cell-material interactions, which enhanced N2a proliferation and triggered the formation of focal adhesions and neural

extensions, occurred at a higher extent on needle-like topographical surfaces, especially SC-125 samples compared to the control surface.
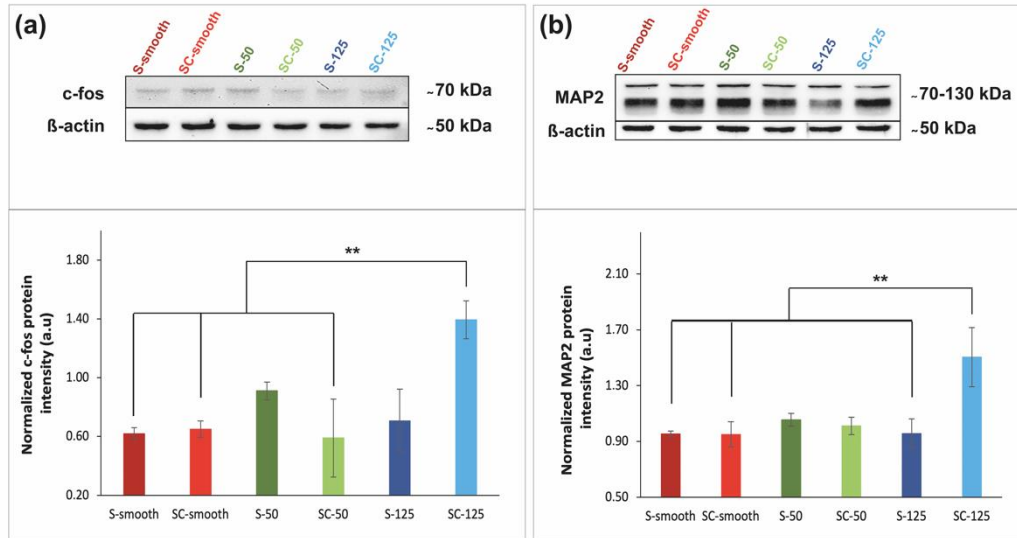
Figure 24. Immunoblot images of c-fos and MAP2 in N2a cells. a) N2a cells on all silk fibroin and silk fibroin-CNF samples were analyzed for c-fos levels using anti-c-fos , and normalized c-fos protein intensity was shown for all sample groups, b) N2a cells on all silk fibroin and silk fibroin-CNF samples were analyzed for MAP2 using anti-MAP2 and normalized MAP2 protein intensity was shown for all sample groups The values are mean±SD, n=3, **$p<0.01$. anti-β-actin was used as an internal control.
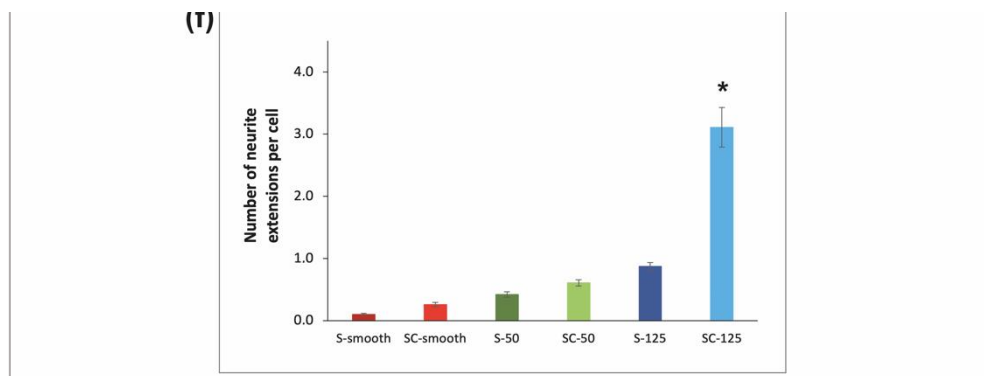
Figure 23. SEM images of N2a cells. a) S-smooth, b) SC-smooth, c) S-50, d) SC-50, e) S-125 and e) SC-125 samples. f) Number of neurite extension per cell for the all sample groups. Number of neurite extensions were statistically significant higher for SC-125 samples compared to all groups. The values are mean±SD, n=5, *$p<0.05$.

Since c-fos protein has a key role in mitogen-activated protein kinase (MAPK) cascade mechanism, which maintains and controls the cellular proliferation, differentiation, and migration, and its expression is vital for firing neurons [85], its expression levels were determined by Western blot to assess N2a cellular activity. As seen in Fig. 24a, the normalized intensity values for c-fos protein expressions were 0.62±0.07, 0.65±0.10, 0.91±0.10, 0.59±0.46, 0.70±0.37 and 1.39±0.22 (a.u) S-smooth, SC-smooth, S-50, SC-50, S-125 and SC-125, respectively. Western blot results showed that cells cultured on SC-125 films had higher c-fos protein expression compared to the S-smooth, SC-smooth and SC-50 groups (Fig. 24a, *$p<0.05$).

Besides, microtubule-associated protein 2 (MAP2) expression levels were determined by Western blot to assess microtubule bundle formation and stability. Since MAP2 proteins are related with neurite outgrowth and also are vital for neuronal plasticity which is the ability of the nervous system, brain to make changes its functions, structures by reorganization based on the different types of stimuli [96]. Fig. 24b shows the normalized intensity values for MAP2 protein expressions that they were 0.95±0.04, 0.95±0.16, 1.05±0.08, 1.01±0.11, 0.96±0.18 and 1.50±0.37 (a.u) S-smooth, SC-smooth, S-50, SC-50, S-125 and SC-125, respectively. Western blot results showed that cells cultured on SC-125 films had statistically significant higher c-fos protein expression compared to the S-smooth, SC-smooth and S-125 groups (Fig. 24b, *$p<0.05$).

4.2   Discussion

In biomedical applications, surface modifications with designing nanotopographies and having conductivity are resulted with enhancing cellular functions for different cell types such as epithelial cells, cardiac cells and stem

cells, etc. [97–99]. In this study, needle-like topographical structures having 50 and 125 nm lateral sizes were formed on a natural polymer silk fibroin and conductive silk fibroin-CNF films, then the effects of these surface topographies and conductivity on N2a cellular functions were investigated. N2a cells showed enhanced cellular functions on having conductive and needle-like topographical surfaces, especially on SC-125 samples. Results suggested that N2a cells sensed these topographical changes and also conductive properties for their activities. This was in-line with the literature where changes in topographical surfaces and having conductivity enhanced cellular responses. For instance, coated with ECM molecules and uncoated nanotopographical (2000, 1000 and 800 nm) surfaces were evaluated with mouse corneal epithelial cells (MCEC) and it was found for the uncoated nanotopographical surfaces that correlated with 50-fold increase in spreading MCEC number and 2-fold increase in focal adhesions on 800 nm surfaces compared to the control flat surfaces [99]. When cardiomyocytes were evaluated on 800 nm x 800 nm x 600 nm (groove width x ridge width x ridge height) conductive silk-polypyrrole (PPy) composite surfaces, it was found that sarcomere length significantly increased on conductive patterned surfaces compared to non-conductive patterned surfaces. Additionally, cardiac maturation marker hMYH7 expression increased nearly 2-fold on conductive patterned surfaces compared to non-conductive patterned ones [98]. In our study, N2a cellular proliferation increased for all needle-like topographical groups at 1st, 3rd and 7th days. Nevertheless, only the cellular proliferation for SC-50 and SC-125 groups were statistically significant than the SC-smooth samples. This increase in cellular proliferation can be explained with the experimental results of other groups on the synergistic effect with topographical surface and conductivity observed which is in-line with literature findings [100].

Our results showed that N2a cells had higher cellular proliferation, higher number of neural extensions, higher focal adhesions based on vinculin expression, up-regulated

c-fos and MAP2 expression levels on conductive needle-like topographical groups, especially SC-125 sample groups as stated consistent with in the literature where with topography and conductivity enhanced cellular functions. MAP2 expression levels confirmed that SC-125 film samples enhanced microtubule formation and stability compared to smooth samples and these results were similar with the literature. For instance, nano and microscale porous structures were fabricated on platinum surfaces and these surfaces were also coated with laminin, collagen type I, poly-D-lysine and collagen-poly-D-lysine, then evaluated on pre-differentiated PC-12 cells and detected moreover that topographical structures increased MAP2 expression even without coating of PC-12 cells [103]. Also, additionally poly(3-hexylthiophene) (P3HT)/PLGA composite membranes were doped with different $FeCl_3$ levels to make conductive membranes. The conductivity enhanced the neurite length of PC12 cells compared to non-conductive material and the expression level of MAP2 showed significant increase while the conductivity was increasing [104]. Similarly, neurite length was higher for SC-125 surfaces than the other groups with both higher rms values and conductivity. In our study, the focal adhesion protein vinculin expression levels were determined the highest level for SC-125 samples compared to other sample groups which was aligned with other studies [99,105]. Yang et al., 2017 showed that Ti-coated nanopatterned substrate promoted the percentage of vinculin positive cells compared to Ti-coated flat substrate, since nanopatterned surfaces mimics the ECM[106]. We also found that c-fos expression levels which were related with neuronal activity were statistically significantly higher for SC-125 groups compared to both type of smooth surfaces and SC-50 sample groups which was also concurrent with the literature [100,107]. These results confirmed that SC-125 film samples enhanced N2a cellular functions compared to smooth samples.

To recapitulate, our results confirmed that needle-like topographical structures with nearly 100 nm features on conductive surfaces may provide positive impacts on the proliferation, focal adhesion, cellular activity, neurite extensions of neuron-like cells. These findings are expected to provide significant contributions to the improvement of implant materials used in neural interface interactions. As an interdisciplinary

study, it was aimed to pave the way for the future application of the material to be developed for the PNS damages.

CHAPTER 5

CONCLUSION

In this thesis, the effects of nanoscale topographies on neural-like cells were evaluated for their future use in NGCs applications. The synergistic effects of nanoscale topographies and conductivity were evaluated to distinguish their effects on neural cells for their promising future use. For this purpose, nanoscale arrays having different sizes were fabricated on PLGA films via replica molding technique to investigate the effects of nanoscale topographies on neural cell functions (Chapter 3). For the replica molding process, 316L SS molds having different nanopit lateral diameters (32 ± 1 nm and 79 ± 0.5 nm) were used. The SEM and AFM analysis confirmed the successful transfer of nanoscale topographies from the molds onto the PLGA films. XPS and FTIR analysis did not reveal presence of an oxide layer or left-over solvent for the PLGA films. Protein adsorption studies revealed enhanced adsorption of proteins onto nanoscale PLGA compared to the control samples. Importantly, N2a cells cultured on nanoscale PLGA films exhibited enhanced proliferation and higher number of neurite extensions, and at the same time, up-regulated c-fos protein expression compared to the ones cultured on the control samples. Cumulatively, the results revealed that fabrication of nanoscale arrays on PLGA films could be promising for NGC applications.

In Chapter 4, needle-like topographies having different sizes were fabricated on both silk fibroin and conductive silk fibroin-CNF films via replica molding technique to investigate the synergistic effetcs of topographies and conductivity on neural cell functions. For the replica molding process, AAO molds having different nanopore lateral diameters (47 ± 6 nm and 122 ± 17 nm) were used. The successful transfer of needle-like topographies from the AAO molds onto the all silk fibroin films were confirmed by the SEM and AFM analysis. FTIR analysis revealed that adding CNF and topography did not changed the percentage of β-sheet crystallites, random coil

and α-helix, and also turns and side chains structures on all silk fibroin sample groups plus, these structural orientations were resulted with hydrophobic properties. The independent of protein adsorption and cellular adhesion, conductivity and fabricating needle-like topographies on the silk fibroin films revealed enhanced cellular proliferation compared the control groups. Additionally, topographies (especially higher needle-like ones) and conductivity, as a synergistic effect enhanced higher number of focal adhesions, neurite extensions, and at the same time, up-regulated c-fos and MAP2 protein expression levels compared to the smooth silk fibroin groups. Those results showed that when conductivity and topographies applied on natural silk fibroin surfaces, that would be favorable properties for NGC applications.

As future works considered, the effects of topographies and conductivity may be studied on stem cells differentiation for NGC applications. On the other hand, the most important future work for these newly developed NGCs is *in vivo* evaluation. Performing *in vivo* studies of the fabricated materials is very important in terms of understanding the use of these materials with topographical and conductivity properties for the purpose of treatment in the future. Based on that, this research should be enlarged with investigating for sciatic nerve defects with behavioral analysis, histological analysis of the defect area and electrophysiological properties of regenerated sciatic nerves, etc. Thus, it will be able to give an idea about whether the obtained surfaces can be used as a treatment method.

REFERENCES

1. Ramos KM, Rommelfanger KS, Greely HT, Koroshetz WJ. Neuroethics and the NIH BRAIN Initiative. *J Responsible Innov*. 2018;5(1):122-130. doi:10.1080/23299460.2017.1319035

2. Vijayavenkataraman S. Nerve guide conduits for peripheral nerve injury repair: A review on design, materials and fabrication methods. *Acta Biomater*. 2020;106:54-69. doi:10.1016/j.actbio.2020.02.003

3. Okano H. Neural stem cells and strategies for the regeneration of the central nervous system. *Proc Japan Acad Ser B*. 2010;86(4):438-450. doi:10.2183/pjab.86.438

4. Vela F, Martínez-Chacón G, Ballestín A, Campos J, Sánchez-Margallo F, Abellán E. Animal models used to study direct peripheral nerve repair: A systematic review. *Neural Regen Res*. 2020;15(3):491-502. doi:10.4103/1673-5374.266068

5. Li R, Li D hui, Zhang H yu, Wang J, Li X kun, Xiao J. Growth factors-based therapeutic strategies and their underlying signaling mechanisms for peripheral nerve regeneration. *Acta Pharmacol Sin*. 2020;41(10):1289-1300. doi:10.1038/s41401-019-0338-1

6. Zhang PX, Han N, Kou YH, et al. Tissue engineering for the repair of peripheral nerve injury. *Neural Regen Res*. 2019;14(1):51-58. doi:10.4103/1673-5374.243701

7. Yang Y, Wang K, Gu X, Leong KW. Biophysical Regulation of Cell Behavior—Cross Talk between Substrate Stiffness and Nanotopography. *Engineering*. 2017;3(1):36-54. doi:10.1016/J.ENG.2017.01.014

8. Houshyar S, Bhattacharyya A, Shanks R. Peripheral Nerve Conduit: Materials and Structures. *ACS Chem Neurosci*. 2019;10(8):3349-3365.

doi:10.1021/acschemneuro.9b00203

9. Arslantunali D, Dursun T, Yucel D, Hasirci N, Hasirci V. Peripheral nerve conduits: Technology update. *Med Devices Evid Res*. 2014;7:405-424. doi:10.2147/MDER.S59124

10. Singh A, Shiekh PA, Das M, Seppälä J, Kumar A. Aligned Chitosan-Gelatin Cryogel-Filled Polyurethane Nerve Guidance Channel for Neural Tissue Engineering: Fabrication, Characterization, and in Vitro Evaluation. *Biomacromolecules*. 2018;20(2):662-673. doi:10.1021/acs.biomac.8b01308

11. Huang C, Ouyang Y, Niu H, et al. Nerve guidance conduits from aligned nanofibers: Improvement of nerve regeneration through longitudinal nanogrooves on a fiber surface. *ACS Appl Mater Interfaces*. 2015;7(13):7189-7196. doi:10.1021/am509227t

12. Clements IP, Munson JM, Bellamkonda R V. Neuronal Tissue Engineering. In: *Biomaterials Science*. Elsevier; 2013:1291-1306.

13. Morelli S, Salerno S, Piscioneri A, Rende M, Campana C, De Bartolo L. Membrane Approaches for Liver and Neuronal Tissue Engineering. *Compr Membr Sci Eng*. 2010;3:229-252. doi:10.1016/B978-0-08-093250-7.00016-5

14. Carvalho CR, Reis RL, Oliveira JM. Fundamentals and Current Strategies for Peripheral Nerve Repair and Regeneration. *Adv Exp Med Biol*. 2020;1249:173-201. doi:10.1007/978-981-15-3258-0_12

15. Guo Z, Kofink S, Chen H, Liang J, Grijpma DW, Poot AA. Synthesis and characterization of rGO-graft-poly(trimethylene carbonate) for nerve regeneration conduits. *Biomed Mater*. 2019;14(3). doi:10.1088/1748-605X/ab0269

16. Wu S, Chen M-S, Maurel P, Lee Y, Bunge MB, Arinzeh TL. Aligned Fibrous PVDF-TrFE Scaffolds with Schwann Cells Support Neurite Extension and Myelination In Vitro. *J Neural Eng*. 2018;15(5).

doi:10.1016/j.physbeh.2017.03.040

17.   Sharifi F, Patel BB, Dzuilko AK, Montazami R, Sakaguchi DS, Hashemi N. Polycaprolactone Microfibrous Scaffolds to Navigate Neural Stem Cells. *Biomacromolecules*. 2016;17(10):3287-3297. doi:10.1021/acs.biomac.6b01028

18.   Nectow AR, Marra KG, Kaplan DL. Biomaterials for the Development of Peripheral Nerve Guidance Conduits. *Tissue Eng Part B Rev*. 2012;18(1):40-50. doi:10.1089/ten.teb.2011.0240

19.   Yang Z, Yang Y, Xu Y, et al. Biomimetic nerve guidance conduit containing engineered exosomes of adipose-derived stem cells promotes peripheral nerve regeneration. *Stem Cell Res Ther*. 2021;12(1):1-14. doi:10.1186/s13287-021-02528-x

20.   Kim SM, Lee MS, Jeon J, et al. Biodegradable Nerve Guidance Conduit with Microporous and Micropatterned Poly(lactic-co-glycolic acid)-Accelerated Sciatic Nerve Regeneration. *Macromol Biosci*. 2018;18(12):1-14. doi:10.1002/mabi.201800290

21.   Farokhi M, Mottaghitalab F, Shokrgozar MA, Kaplan DL, Kim HW, Kundu SC. Prospects of peripheral nerve tissue engineering using nerve guide conduits based on silk fibroin protein and other biopolymers. *Int Mater Rev*. 2017;62(7):367-391. doi:10.1080/09506608.2016.1252551

22.   Magaz A, Faroni A, Gough JE, Reid AJ, Li X, Blaker JJ. Bioactive Silk-Based Nerve Guidance Conduits for Augmenting Peripheral Nerve Repair. *Adv Healthc Mater*. 2018;7(23). doi:10.1002/adhm.201800308

23.   Zhang Q, Zhao Y, Yan S, et al. Preparation of uniaxial multichannel silk fibroin scaffolds for guiding primary neurons. *Acta Biomater*. 2012;8(7):2628-2638. doi:10.1016/j.actbio.2012.03.033

24.   Rockwood DN, Preda RC, Yücal T, Wang X, Lovett ML, Kaplan DL.

Materials Fabrication from Bombyx mori Silk Fibroin. *Nat Protoc*. 2011;6(10). doi:10.1038/jid.2014.371

25. Gennari CGM, Cilurzo F, Mitro N, Caruso D, Minghetti P, Magnaghi V. In vitro and in vivo evaluation of silk fibroin functionalized with GABA and allopregnanolone for Schwann cell and neuron survival. *Regen Med*. 2017;13(2):141-157. doi:10.2217/rme-2017-0102

26. Naskar D, Bhattacharjee P, Ghosh AK, Mandal M, Kundu SC. Carbon Nanofiber Reinforced Nonmulberry Silk Protein Fibroin Nanobiocomposite for Tissue Engineering Applications. *ACS Appl Mater Interfaces*. 2017;9(23):19356-19370. doi:10.1021/acsami.6b04777

27. Afjeh-Dana E, Naserzadeh P, Nazari H, et al. Gold nanorods reinforced silk fibroin nanocomposite for peripheral nerve tissue engineering applications. *Int J Biol Macromol*. 2019;129:1034-1039. doi:10.1016/j.ijbiomac.2019.02.050

28. Stout DA, Basu B, Webster TJ. Poly (lactic–co-glycolic acid): carbon nanofiber composites for myocardial tissue engineering applications. *Acta Biomater*. 2011;7(8):3101-3112.

29. Price RL, Waid MC, Haberstroh KM, Webster TJ. Selective bone cell adhesion on formulations containing carbon nanofibers. *Biomaterials*. 2003;24(11):1877-1887. doi:10.1016/S0142-9612(02)00609-9

30. Amani H, Arzaghi H, Bayandori M, et al. Controlling Cell Behavior through the Design of Biomaterial Surfaces: A Focus on Surface Modification Techniques. *Adv Mater Interfaces*. 2019;6(13):1-30. doi:10.1002/admi.201900572

31. Kehoe S, Zhang XF, Boyd D. FDA approved guidance conduits and wraps for peripheral nerve injury: A review of materials and efficacy. *Injury*. 2012;43(5):553-572. doi:10.1016/j.injury.2010.12.030

32. Zarrintaj P, Zangene E, Manouchehri S, et al. Conductive biomaterials as nerve conduits: Recent advances and future challenges. *Appl Mater Today*. 2020;20:100784. doi:10.1016/j.apmt.2020.100784

33. Cavalcante FTT, de A. Falcão IR, da S. Souza JE, et al. Designing of Nanomaterials-Based Enzymatic Biosensors: Synthesis, Properties, and Applications. *Electrochem*. 2021;2(1):149-184. doi:10.3390/electrochem2010012

34. McMurray R, Dalby MJ, Gadegaard N. Nanopatterned surfaces for biomedical applications. In: *Biomedical Engineering, Trends in Materials Science*. ; 2011:375-396. doi:10.5772/992

35. Ma QL, Zhao LZ, Liu RR, et al. Improved implant osseointegration of a nanostructured titanium surface via mediation of macrophage polarization. *Biomaterials*. 2014;35(37):9853-9867. doi:10.1016/j.biomaterials.2014.08.025

36. Ballo A, Agheli H, Lausmaa J, Thomsen P, Petronis S. Nanostructured model implants for in vivo studies: influence of well-defined nanotopography on de novo bone formation on titanium implants. *Int J Nanomedicine*. 2011;6:3415-3428. doi:10.2147/IJN.S25867

37. Lu J, Khang D, Webster TJ. Greater endothelial cell responses on submicron and nanometer rough titanium surfaces. *J Biomed Mater Res - Part A*. 2010;94(4):1042-1049. doi:10.1002/jbm.a.32778

38. Giavaresi G, Tschon M, Daly JH, et al. In vitro and in vivo response to nanotopographically-modified surfaces of poly(3-hydroxybutyrate-co-3-hydroxyvalerate) and polycaprolactone. *J Biomater Sci Polym Ed*. 2006;17(12):1405-1423. doi:10.1163/156856206778937226

39. Oh S, Brammer KS, Li YS, et al. Stem cell fate dictated solely by altered nanotube dimension. *Proc Natl Acad Sci U S A*. 2009;106:2130-2135. doi:10.1073/pnas.0813200106

40. Tuft BW, Li S, Xu L, et al. Photopolymerized microfeatures for directed spiral ganglion neurite and Schwann cell growth. *Biomaterials*. 2013;34(1):42-54. doi:10.1016/j.biomaterials.2012.09.053

41. Clarke JC, Tuft BW, Clinger JD, et al. Micropatterned methacrylate polymers direct spiral ganglion neurite and Schwann cell growth. *Hear Res*. 2011;278(1-2):96-105. doi:10.1016/j.heares.2011.05.004

42. Christopherson GT, Song H, Mao HQ. The influence of fiber diameter of electrospun substrates on neural stem cell differentiation and proliferation. *Biomaterials*. 2009;30(4):556-564. doi:10.1016/j.biomaterials.2008.10.004

43. Yim EKF, Pang SW, Leong KW. Synthetic nanostructures inducing differentiation of human mesenchymal stem cells into neuronal lineage. *Exp Cell Res*. 2007;313(9):1820-1829. doi:10.1016/j.yexcr.2007.02.031

44. Tsuruma A, Tanaka M, Yamamoto S, Shimomura M. Control of neural stem cell differentiation on honeycomb films. *Colloids Surfaces A Physicochem Eng Asp*. 2008;313-314:536-540. doi:10.1016/j.colsurfa.2007.05.079

45. Yang K, Jung K, Ko E, et al. Nanotopographical manipulation of focal adhesion formation for enhanced differentiation of human neural stem cells. *ACS Appl Mater Interfaces*. 2013;5(21):10529-10540. doi:10.1021/am402156f

46. Yang K, Park E, Lee JS, et al. Biodegradable Nanotopography Combined with Neurotrophic Signals Enhances Contact Guidance and Neuronal Differentiation of Human Neural Stem Cells. *Macromol Biosci*. 2015;15(10):1348-1356. doi:10.1002/mabi.201500080

47. Ao Q, Wang A, Cao W, et al. Manufacture of multimicrotubule chitosan nerve conduits with novel molds and characterization in vitro. *J Biomed Mater Res Part A An Off J Soc Biomater Japanese Soc Biomater Aust Soc Biomater Korean Soc Biomater*. 2006;77(1):11-18.

48. Chang YC, Chen MH, Liao SY, et al. Multichanneled Nerve Guidance Conduit with Spatial Gradients of Neurotrophic Factors and Oriented Nanotopography for Repairing the Peripheral Nervous System. *ACS Appl Mater Interfaces*. 2017;9(43):37623-37636. doi:10.1021/acsami.7b12567

49. Ganguly D, Johnson CDL, Gottipati MK, Rende D, Borca-Tasciuc DA, Gilbert RJ. Specific Nanoporous Geometries on Anodized Alumina Surfaces Influence Astrocyte Adhesion and Glial Fibrillary Acidic Protein Immunoreactivity Levels. *ACS Biomater Sci Eng*. 2018;4(1):128-141. doi:10.1021/acsbiomaterials.7b00760

50. Farokhi M, Mottaghitalab F, Saeb MR, et al. Conductive Biomaterials as Substrates for Neural Stem Cells Differentiation towards Neuronal Lineage Cells. *Macromol Biosci*. 2021;21(1):1-22. doi:10.1002/mabi.202000123

51. Wang Y, Zhang Y, Zhang Z, et al. An injectable high-conductive bimaterial scaffold for neural stimulation. *Colloids Surfaces B Biointerfaces*. 2020;195(June):111210. doi:10.1016/j.colsurfb.2020.111210

52. Park J, Jeon J, Kim B, et al. Electrically Conductive Hydrogel Nerve Guidance Conduits for Peripheral Nerve Regeneration. *Adv Funct Mater*. 2020;30(39):1-14. doi:10.1002/adfm.202003759

53. Arslantunali D, Dursun T, Yucel D, Hasirci N, Hasirci V. Peripheral nerve conduits: technology update. *Med Devices Evid Res*. 2014;1(7):405-424. doi:10.2147/MDER.S59124

54. Nawrotek K. Current Approaches to Peripheral Nervous Tissue Regeneration – Mimicking Nature. A review. *J Res Innov Nat Med Heal Sci*. 2015;1(1):16-33. http://www.researchininnovation.com/index.php/naturalsciences/article/view/JRI013.

55. Nelson DL, Cox MM. *Lehninger's Principles of Biochemistry*.; 2013. doi:10.1017/CBO9781107415324.004

56. Hochman-Mendez C, Cantini M, Moratal D, Salmeron-Sanchez M, Coelho-Sampaio T. A fractal nature for polymerized laminin. *PLoS One*. 2014;9(10). doi:10.1371/journal.pone.0109388

57. Koteliansky VE, Glukhova MA, Benjamin M V., et al. A Study of the Structure of Fibronectin. *Eur J Biochem*. 1981;119(3):619-624. doi:10.1111/j.1432-1033.1981.tb05652.x

58. Paulsson M, Yurchenco PD, Ruben GC, Engel J, Timpl R. Structure of low density heparan sulfate proteoglycan isolated from a mouse tumor basement membrane. *J Mol Biol*. 1987;197(2):297-313. doi:10.1016/0022-2836(87)90125-2

59. Zhang B, Ni H, Chen R, et al. A two-step anodic method to fabricate self-organised nanopore arrays on stainless steel. *Appl Surf Sci*. 2015;351:1161-1168. doi:10.1016/j.apsusc.2015.06.083

60. Carpenter J, Khang D, Webster TJ. Nanometer polymer surface features: the influence on surface energy, protein adsorption and endothelial cell adhesion. *Nanotechnology*. 2008;19(50):505103. doi:10.1088/0957-4484/19/50/505103

61. Tufan Y, Öztatlı H, Garipcan B, Ercan B. Development of electrically conductive porous silk fibroin/carbon nanofiber scaffolds. *Biomed Mater*. 2021;16(2). doi:10.1088/1748-605X/abc3db

62. Hu X, Kaplan D, Cebe P. Determining beta-sheet crystallinity in fibrous proteins by thermal analysis and infrared spectroscopy. *Macromolecules*. 2006;39(18):6161-6170. doi:10.1021/ma0610109

63. LePage KT, Dickey RW, Gerwick WH, Jester EL, Murray TF. On the use of neuro-2a neuroblastoma cells versus intact neurons in primary culture for neurotoxicity studies. *Crit Rev Neurobiol*. 2005;17(1):27-50. doi:10.1615/CritRevNeurobiol.v17.i1.20

64. Salto R, Vílchez JD, Girón MD, et al. β-Hydroxy-β-methylbutyrate (HMB) promotes neurite outgrowth in Neuro2a cells. *PLoS One*. 2015;10(8):1-13. doi:10.1371/journal.pone.0135614

65. Riboni L, Prinetti A, Bassi R, Caminiti A, Tettamanti G. A mediator role of ceramide in the regulation of neuroblastoma neuro2a cell differentiation. *J Biol Chem*. 1995;270(45):26868-26875. doi:10.1074/jbc.270.45.26868

66. Miller DC, Haberstroh KM, Webster TJ. PLGA nanometer surface features manipulate fibronectin interactions for improved vascular cell adhesion. *Wiley Intersci*. 2006;81(3):678-684. doi:10.1002/jbm.a

67. Ronn LCB, Ralets I, Hartz BP, et al. A simple procedure for quantification of neurite outgrowth based on stereological principles. *J Neurosci Methods*. 2000;100(1-2):25-32. doi:10.1016/S0165-0270(00)00228-4

68. Pemberton K, Mersman B, Xu F. Using ImageJ to Assess Neurite Outgrowth in Mammalian Cell Cultures: Research Data Quantification Exercises in Undergraduate Neuroscience Lab. *J Undergrad Neurosci Educ*. 2018;16(2):A186-A194. http://www.ncbi.nlm.nih.gov/pubmed/30057501%0Ahttp://www.pubmedcentral.nih.gov/articlerender.fcgi?artid=PMC6057772.

69. Mahmood T, Yang P-C. Western blot: Technique, theory, and trouble shooting. *N Am J Med Sci*. 2012;4(9):429-434. doi:10.4103/1947-2714.100998

70. Yang D, Lü X, Hong Y, Xi T, Zhang D. The molecular mechanism of mediation of adsorbed serum proteins to endothelial cells adhesion and growth on biomaterials. *Biomaterials*. 2013;34(23):5747-5758. doi:10.1016/j.biomaterials.2013.04.028

71. Bradford MM. A rapid and sensitive method for the quantitation of microgram quantities of protein utilizing the principle of protein-dye binding. *Anal Biochem*. 1976;72:248-254. doi:10.1016/j.cj.2017.04.003

72. Yang K, Yu SJ, Lee JS, et al. Electroconductive nanoscale topography for enhanced neuronal differentiation and electrophysiological maturation of human neural stem cells. *Nanoscale*. 2017;9(47):18737-18752. doi:10.1039/c7nr05446g

73. Engel J, Odermatt E, Engel A, et al. Shapes, domain organizations and flexibility of laminin and fibronectin, two multifunctional proteins of the extracellular matrix. *J Mol Biol*. 1981;150(1):97-120. doi:10.1016/0022-2836(81)90326-0

74. Torres-Lagares D, Castellanos-Cosano L, Serrera-Figallo M ángeles, et al. In vitro and in vivo study of poly(lactic-co-glycolic) (PLGA)membranes treated with oxygen plasma and coated with nanostructured hydroxyapatite ultrathin films for guided bone regeneration processes. *Polymers (Basel)*. 2017;9(9). doi:10.3390/polym9090410

75. Cangellaris O V., Gillette MU. Biomaterials for Enhancing Neuronal Repair. *Front Mater*. 2018;5(21):1-8. doi:10.3389/fmats.2018.00021

76. Wang GJ, Lin YC, Li CW, Hsueh CC, Hsu SH, Hung HS. Fabrication of orderly nanostructured PLGA scaffolds using anodic aluminum oxide templates. *Biomed Microdevices*. 2009;11(4):843-850. doi:10.1007/s10544-009-9301-0

77. Ni S, Sun L, Ercan B, Liu L, Ziemer K, Webster TJ. A mechanism for the enhanced attachment and proliferation of fibroblasts on anodized 316L stainless steel with nano-pit arrays. *J Biomed Mater Res - Part B Appl Biomater*. 2014;102(6):1297-1303. doi:10.1002/jbm.b.33127

78. Coates J. Interpretation of Infrared Spectra, A Practical Approach. In: *Encyclopedia OfAnalytical Chemistry*. ; 2000:10815-10837. doi:10.1097/00007611-198402000-00017

79. Movasaghi Z, Rehman S, Rehman IU. Fourier Transform Infrared (FTIR) Spectroscopy of Biological Tissues. *Appl Spectrosc Rev*. 2008;43(2):134-

179. doi:10.1080/05704920701829043

80.   Ngandu Mpoyi E, Cantini M, Reynolds PM, Gadegaard N, Dalby MJ, Salmerón-Sánchez M. Protein Adsorption as a Key Mediator in the Nanotopographical Control of Cell Behavior. *ACS Nano*. 2016;10(7):6638-6647. doi:10.1021/acsnano.6b01649

81.   Scopelliti PE, Borgonovo A, Indrieri M, et al. The effect of surface nanometre-scale morphology on protein adsorption. *PLoS One*. 2010;5(7):1-9. doi:10.1371/journal.pone.0011862

82.   Hou Y, Xie W, Yu L, et al. Surface Roughness Gradients Reveal Topography-Specific Mechanosensitive Responses in Human Mesenchymal Stem Cells. *Small*. 2020;16(10). doi:10.1002/smll.201905422

83.   Mohan CC, Sreerekha PR, Divyarani V V., Nair S, Chennazhi K, Menon D. Influence of titania nanotopography on human vascular cell functionality and its proliferation in vitro. *J Mater Chem*. 2012;22(4):1326-1340. doi:10.1039/c1jm13726c

84.   Zhou Q, Xie J, Bao M, et al. Engineering aligned electrospun PLLA microfibers with nano-porous surface nanotopography for modulating the responses of vascular smooth muscle cells. *J Mater Chem B*. 2015;3(21):4439-4450. doi:10.1039/c5tb00051c

85.   Bullitt E. Expression of C- fos- like protein as a marker for neuronal activity following noxious stimulation in the rat. *J Comp Neurol*. 1990;296(4):517-530. doi:10.1002/cne.902960402

86.   Sjöström T, Dalby MJ, Hart A, Tare R, Oreffo ROC, Su B. Fabrication of pillar-like titania nanostructures on titanium and their interactions with human skeletal stem cells. *Acta Biomater*. 2009;5(5):1433-1441. doi:10.1016/j.actbio.2009.01.007

87.   Castro-Raucci LMS, Francischini MS, Teixeira LN, et al. Titanium with

Nanotopography Induces Osteoblast Differentiation by Regulating Endogenous Bone Morphogenetic Protein Expression and Signaling Pathway. *J Cell Biochem*. 2016;117(7):1718-1729. doi:10.1002/jcb.25469

88. Schaub NJ, D'Amato AR, Mason A, et al. The effect of engineered nanotopography of electrospun microfibers on fiber rigidity and macrophage cytokine production. *J Biomater Sci Polym Ed*. 2017;28(13):1303-1323. doi:10.1080/09205063.2017.1321345

89. Brunetti V, Maiorano G, Rizzello L, et al. Neurons sense nanoscale roughness with nanometer sensitivity. *Proc Natl Acad Sci U S A*. 2010;107(14):6264-6269. doi:10.1073/pnas.0914456107

90. Khorasani MT, Mirzadeh H, Irani S. Plasma surface modification of poly (l-lactic acid) and poly (lactic-co-glycolic acid) films for improvement of nerve cells adhesion. *Radiat Phys Chem*. 2008;77(3):280-287. doi:10.1016/j.radphyschem.2007.05.013

91. Sadeghi A, Moztarzadeh F, Aghazadeh Mohandesi J. Investigating the effect of chitosan on hydrophilicity and bioactivity of conductive electrospun composite scaffold for neural tissue engineering. *Int J Biol Macromol*. 2019;121:625-632. doi:10.1016/j.ijbiomac.2018.10.022

92. Ercan B, Khang D, Carpenter J, Webster TJ. Using mathematical models to understand the effect of nanoscale roughness on protein adsorption for improving medical devices. *Int J Nanomedicine*. 2013;8(SUPPL. 1):75-81. doi:10.2147/IJN.S47286

93. Li M, Mondrinos MJ, Chen X, Gandhi MR, Ko FK, Lelkes PI. Elastin Blends for Tissue Engineering Scaffolds. *J Biomed Mater Res Part A*. 2006;79(4):963-973. doi:10.1002/jbm.a

94. López-Cebral R, Silva-Correia J, Reis RL, Silva TH, Oliveira JM. Peripheral Nerve Injury: Current Challenges, Conventional Treatment Approaches, and New Trends in Biomaterials-Based Regenerative Strategies. *ACS Biomater*

Sci Eng. 2017;3(12):3098-3122. doi:10.1021/acsbiomaterials.7b00655

95. Chiono V, Tonda-Turo C. Trends in the design of nerve guidance channels in peripheral nerve tissue engineering. *Prog Neurobiol*. 2015;131:87-104. doi:10.1016/j.pneurobio.2015.06.001

96. Dõâ J, Avila J, Sa C. Phosphorylation of microtubule-associated protein 2 (MAP2) and its relevance for the regulation of the neuronal cytoskeleton function. *Prog Neurobiol*. 2000;61:133-168.

97. Manchineella S, Thrivikraman G, Basu B, Govindaraju T. Surface-functionalized silk fibroin films as a platform to guide neuron-like differentiation of human mesenchymal stem cells. *ACS Appl Mater Interfaces*. 2016;8(35):22849-22859. doi:10.1021/acsami.6b06403

98. Tsui JH, Ostrovsky-Snider NA, Yama DMP, et al. Conductive silk-polypyrrole composite scaffolds with bioinspired nanotopographic cues for cardiac tissue engineering. *J Mater Chem B*. 2018;6(44):7185-7196. doi:10.1039/C8TB01116H

99. Luo Y, Kang KB, Sartaj R, et al. Silk films with nanotopography and extracellular proteins enhance corneal epithelial wound healing. *Sci Rep*. 2021;11(1):1-15. doi:10.1038/s41598-021-87658-1

100. Eftekhari BS, Eskandari M, Janmey PA, Samadikuchaksaraei A, Gholipourmalekabadi M. Surface Topography and Electrical Signaling: Single and Synergistic Effects on Neural Differentiation of Stem Cells. *Adv Funct Mater*. 2020;30(25):1-17. doi:10.1002/adfm.201907792

101. Tretinnikov ON, Tamada Y. Influence of casting temperature on the near-surface structure and wettability of cast silk fibroin films. *Langmuir*. 2001;17(23):7406-7413. doi:10.1021/la010791y

102. Ferrari M, Cirisano F, Carmen Morán M. Mammalian cell behavior on hydrophobic substrates: Influence of surface properties. *Colloids and*

Interfaces. 2019;3(2). doi:10.3390/colloids3020048

103.   Schlie-Wolter S, Deiwick A, Fadeeva E, Paasche G, Lenarz T, Chichkov
       BN. Topography and coating of platinum improve the electrochemical
       properties and neuronal guidance. *ACS Appl Mater Interfaces*.
       2013;5(3):1070-1077. doi:10.1021/am3028487

104.   Zhang S, Yan H, Yeh JM, Shi X, Zhang P. Electroactive Composite of
       FeCl3-Doped P3HT/PLGA with Adjustable Electrical Conductivity for
       Potential Application in Neural Tissue Engineering. *Macromol Biosci*.
       2019;19(10):1-11. doi:10.1002/mabi.201900147

105.   Cho YW, Kim DS, Suhito IR, Han DK, Lee T, Kim TH. Enhancing
       neurogenesis of neural stem cells using homogeneous nanohole pattern-
       modified conductive platform. *Int J Mol Sci*. 2020;21(1):1-15.
       doi:10.3390/ijms21010191

106.   Yang K, Yu SJ, Lee JS, et al. Electroconductive nanoscale topography for
       enhanced neuronal differentiation and electrophysiological maturation of
       human neural stem cells. *Nanoscale*. 2017;9(47):18737-18752.
       doi:10.1039/c7nr05446g

107.   Sudwilai T, Ng JJ, Boonkrai C, Israsena N, Chuangchote S, Supaphol P.
       Polypyrrole-coated electrospun poly(lactic acid) fibrous scaffold: Effects of
       coating on electrical conductivity and neural cell growth. *J Biomater Sci
       Polym Ed*. 2014;25(12):1240-1252. doi:10.1080/09205063.2014.926578

108.   Xu G, Gong L, Yang Z, Liu XY. What makes spider silk fibers so strong?
       from molecular-crystallite network to hierarchical network structures. *Soft
       Matter*. 2014;10(13):2116-2123. doi:10.1039/c3sm52845f

109.   Endo M, Kim YA, Hayashi T, et al. Structural characterization of cup-
       stacked-type nanofibers with an entirely hollow core. *Appl Phys Lett*.
       2002;80(7):1267-1269. doi:10.1063/1.1450264

110. Nawrotek K. Current Approaches to Peripheral Nervous Tissue Regeneration – Mimicking Nature. *J Res Innov Nat Med Heal Sci*. 2015;1(1):16-33. http://www.researchininnovation.com/index.php/naturalsciences/article/view /JRI013.

CURRICULUM VITAE

Surname, Name: Mimiroğlu, Didem

EDUCATION

Degree	Institution	Year of Graduation
MS	Ankara University, Biotechnology	2015
BS	Ege University, Biochemistry	2013
High School	Muğla Anadolu High School, Muğla	2008

WORK EXPERIENCE

Year	Place	Enrollment
2015-present	METU	Research Assistant
2018-2019	DN Biyomed Life Sciences Company	Co-founder and company manager
2015	Cumhuriyet University	Research Assistant

FOREIGN LANGUAGES

Advanced English

PUBLICATIONS

1. Mimiroglu, D., Yanik, T., & Ercan, B. (2022). Nanophase surface arrays on poly (lactic- co- glycolic acid) upregulate neural cell functions. Journal of Biomedical Materials Research Part A, 110(1), 64-75.

2. Uslu, E., Mimiroglu, D., & Ercan, B. (2021). Nanofeature size and morphology of tantalum oxide surfaces control osteoblast functions. ACS Applied Bio Materials, 4(1), 780-794.

HOBBIES

Yoga, Pilates, Trekking, Cooking, Writing, Art